

**INVESTIGATION OF STRUCTURAL, ELECTRICAL,
DIELECTRIC PROPERTIES OF MIXED AND TETRAGONAL
GARNET PHASES OF $\text{Li}_7\text{La}_3\text{Zr}_2\text{O}_{12}$ (LLZO)**

A DISSERTATION
SUBMITTED IN PARTIAL FULFILLMENT OF THE REQUIREMENTS
FOR THE AWARD OF THE DEGREE
OF

**MASTER OF SCIENCE
IN
PHYSICS**

Submitted by:

Ujjawal Sagar (2K19/MSCPHY/11)

Sharad Singh Jadaun (2K19/MSCPHY/09)

Under the supervision of

DR. AMRISH K. PANWAR



DEPARTMENT OF APPLIED PHYSICS

DELHI TECHNOLOGICAL UNIVERSITY

(Formerly Delhi College of Engineering)

Bawana Road, Delhi-110042

MAY, 2021

DELHI TECHNOLOGICAL UNIVERSITY

(Formerly Delhi College of Engineering)

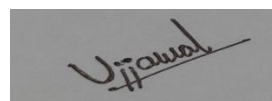
Bawana Road, Delhi-110042

CANDIDATE'S DECLARATION

We, Ujjawal Sigar (2K19/MSCPHY/11) and Sharad Singh Jadaun (2K19/MSCPHY/09), students MSc(Physics), hereby declare that the project Dissertation titled “Investigation of structural, electrical, dielectric properties of mixed and tetragonal garnet phase of $\text{Li}_7\text{La}_3\text{Zr}_2\text{O}_{12}$ (LLZO)” which is submitted by us to the Department of Applied Physics, Delhi Technological University, Delhi in partial fulfillment of the requirement for the award of the degree of Master of Science, is original and not copied from any source without proper citation. This work has not previously formed the basis for the award of any Degree, Diploma Associateship, Fellowship or other similar title or recognition.

Place: Delhi

Date: 30 May 2021



Ujjawal Sigar



Sharad Singh Jadaun

DEPARTMENT OF APPLIED PHYSICS

DELHI TECHNOLOGICAL UNIVERSITY

(Formerly Delhi College of Engineering)

Bawana Road, Delhi-110042

CERTIFICATE

I hereby certify that the Project Dissertation titled “Investigation of structural, electrical, dielectric properties of mixed and tetragonal garnet phase of $\text{Li}_7\text{La}_3\text{Zr}_2\text{O}_{12}$ (LLZO)” which is submitted by, Ujjawal Sagar (2K19/MSCPHY/11) and Sharad Singh Jadaun (2K19/MSCPHY/09), Department of Applied Physics, Delhi Technological University, Delhi in partial fulfillment of the requirement for the award of the degree of Master of Science, is a record of the project work carried out by the students under my supervision. To the best of my knowledge this work has not been submitted in part or full for any Degree or Diploma to this University or elsewhere.

Place: Delhi


Dr. Amrish K. Panwar

Date: 30 May 2021

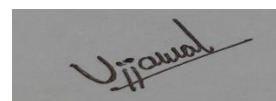
SUPERVISOR

ABSTRACT

In this study, two different phases of $\text{Li}_7\text{La}_3\text{Zr}_2\text{O}_{12}$ (LLZO) i.e mixed(tetragonal garnet and cubic) and tetragonal garnet has been synthesized using a solid-state reaction route at low sintering temperature and different sintering times. X-ray diffraction (XRD) analysis has been carried out to confirm the formation of a mixed phase of tetragonal garnet and cubic structure and tetragonal garnet. The structural, physico-chemical, electrical, and dielectric characterization of synthesized LLZO are performed. The average crystallite size and strain have been estimated from the XRD peaks analysis using the Williamson-Hall method. Field Emission Scanning Electron Microscope (FE-SEM) micrographs reveal slightly agglomerated and dense layer-like staircase kind of morphology in the mixed-phase and sheet-like porous structure for the tetragonal garnet at the nanolevel. The impedance spectroscopy data has been recorded at various temperatures from 303 K to 373 K over a frequency range of 70 kHz to 5 MHz. The electrical analysis indicates that charges possess the classical hopping mechanism for conduction. A.C. activation energy of mixed and tetragonal garnet phase of LLZO has been observed at a lower frequency of 70 kHz and it is noticed nearly of same order (0.16 eV). Dielectric results show the presence of space charge polarization in the external electric field which consists of hopping polarization in the bulk and interfacial polarization (Maxwell-Wagner polarization) at the grain boundaries in both the phases. The strength of polarization is seen as greater in the tetragonal garnet phase of LLZO.

ACKNOWLEDGMENT

Firstly, and importantly, we would like to thank our supervisor Dr. Amrish K. Panwar for allowing and giving us the golden opportunity to work in his Lithium-Ion Battery Technology Lab. Without his mentoring and unconditional support, this work would not have been possible. We would like to thank him for his valuable time and his feedback and suggestions. We sincerely thank him for his patience in correcting manuscripts and hope to carry forward the various nuances we learned during the writing process. His approach to scientific inquiry kept the joy of research alive during this thesis. Further, we would like to thank all the Ph.D. scholars in our lab to provide us healthy environment: Abhishek Bhardwaj, Shivani Rajput, Anchali Jain, and Snigdha Sharma. The success of work depends upon the nature of the working environment. We also extend our thanks to all the faculty members, M.Sc.(Physics) scholars and members of the Department of Applied Physics, Delhi Technological University for their suggestions and valued support. Lastly, we would also like to thank our parents for their enduring support and for believing in us always.



Ujjawal Sagar



Sharad Singh Jadaun

CONTENTS

Candidate's Declaration	i
Certificate	ii
Abstract	iii
Acknowledgment	iv
Contents	v
List of Tables	vii
List of Figures	ix
CHAPTER 1 INTRODUCTION AND LITERATURE REVIEW	1
1.1 Introduction	1
1.2 History of battery	1
1.3 Working principle of Battery	2
1.4 Solid-State Lithium-Ion Battery and Solid Electrolyte	3
1.5 Lithium Lanthanum Zirconium Oxide ($\text{Li}_7\text{La}_3\text{Zr}_2\text{O}_{12}$)	4
1.6 Doping	6
1.7 Challenges	6
1.8 Objective of the Research Work	7
CHAPTER 2 CHARACTERIZATION TECHNIQUES	8
2.1 X-Ray Diffraction (XRD)	8

2.2 Scanning Electron Microscopy (SEM)	9
2.3 Thermal Gravimetric Analysis (TGA)	10
CHAPTER 3 SYNTHESIS OF TETRAGONAL (GARNET) AND MIXED-PHASE OF LLZO	11
3.1 Introduction	11
3.2 Experimental	11
3.2.1 Material Synthesis	11
3.2.2 Material Characterization	12
3.3 Result and Discussion	12
3.3.1 Thermal Analysis	12
3.3.2 Structural and Morphological Analysis	13
CHAPTER 4 STUDY OF ELECTRICAL AND DIELECTRIC PROPERTIES OF MIXED AND TETRAGONAL GARNET PHASE OF LLZO	18
4.1 Introduction	18
4.2 Experimental	18
4.2.1 Pellet Formation and Polishing	18
4.2.2 Material Characterization	19
4.3 Result and Discussion	20
4.3.1 Electrical Measurement	20
4.3.2 Dielectric Measurement	25

CHAPTER 5 CONCLUSION AND FUTURE WORK	28
REFERENCES	30

LIST OF FIGURES

Figure 1.1 Schematic of a Li-ion battery with liquid electrolyte.....	3
Figure 1.2 Tetragonal garnet LLZO.....	5
Figure 2.1 Schematic illustration of Bragg's law.....	8
Figure 2.2 Schematic explanation of the origin of secondary electrons (SE) and backscattered electrons (BSE).....	9
Figure 3.1 TGA and DSC curves of LLZO under air atmosphere.....	13
Figure 3.2. (a) XRD pattern and (b) Williamson-Hall plot of as-synthesized LLZO at calcination temperature of 700 °C for 10 hours in air atmosphere.....	14
Figure 3.3. (a) XRD pattern and (b) Williamson-Hall plot of as-synthesized LLZO at calcination temperature of 700 °C for 8 hours in air atmosphere.....	15
Figure 3.4. SEM image of mixed-phase of LLZO, sintered for 10hr (a)5µm (b)400nm..	16
Figure 3.5. SEM image of tetragonal garnet of LLZO, sintered for 8hr (a)5µm (b)400nm.	17
Figure 4.1 AC conductivity versus the frequency at the temperature range of 30 °C to 100 °C, (a) mixed-phase (b) tetragonal(garnet) of LLZO.....	21
Figure 4.2 Arrhenius plot, variation of conductivity with temperature for as-synthesized LLZO, (a) mixed-phase (b) tetragonal(garnet).....	24
Figure 4.3. Dielectric constant versus the logarithm of frequency at various temperatures, (a) mixed-phase (b) tetragonal garnet.....	26
Figure 4.4. Dielectric loss versus the logarithm of frequency at various temperatures, (a) mixed-phase (b) tetragonal garnet.....	27

LIST OF TABLES

Table 4.1. The calculated value of n and A of mixed-phase at different temperatures.....**22**

Table 4.2. The calculated value of n and A of tetragonal(garnet) at different temperatures..... **22**

CHAPTER 1

INTRODUCTION AND LITERATURE REVIEW

1.1 INTRODUCTION

In recent years, the storage of energy in the electricity and energy sectors becomes highly valuable. Energy storage plays a critical role in providing uninterrupted power with constant frequency to all electrical appliances. Annually, the need for renewable energy resources like wind and solar power is increasing at a high pace. To encounter the global warming problem, the world is shifting towards the electrification of the transportation sector which leads to the domination of electric vehicles. But renewable energy and electrification of transportation are highly dependent on the energy storage facility. The development of electricity storage facilities on large scale provides a rapid shifting from non-renewable to renewable sources for energy consumption.

1.2 HISTORY OF BATTERY

In the 1749s, while experimenting with electricity, Benjamin Franklin who was the founding father and U.S. polymath used the term “Battery” to explain a series of linked capacitors. Further in the 1800s, the first very true acknowledged battery names Voltaic pile was invented by Alessandro Volta which consists of piled pair of Zinc and copper discs piled of each other, where the layer of cloth was used as electrolyte. Voltaic pile battery faced some problems like short-circuiting and electrolyte leaking. After 60 years of the voltaic pile, the first-ever rechargeable battery based on a lead-acid system was invented by Gaston Plante. These types of lead-acid batteries are heavy and are still in use where weight is not an issue. Because of their appreciable lifetime and durability, these batteries are used even in today’s world. Later in 1899, the first alkaline battery i.e. nickel-cadmium battery was invented by Waldemar Jungner who was a Swedish scientist. Components of these type of batteries are potassium hydroxide, nickel and cadmium

electrode. The higher capacities and stability for longer periods leads to the commercialization of these batteries in the early 19th century. Further, these batteries are studied by improvising the electrode material. Finally, in the 1970s, lithium-ion batteries come into the market although experimentation over these batteries was initiated in 1912. Li-ion batteries are the most promising batteries since it includes Li chemistry which has advantages such as:

- (i) Small ionic radius and lightest element which leads to the higher energy density of Li-containing materials.
- (ii) Lowest reduction potential which provides higher voltages between electrodes.

1.3 WORKING PRINCIPLE OF BATTERY

There are three important components of a rechargeable battery/cell i.e. cathode (positive electrode), electrolyte, and anode (negative electrode) as shown in Figure 1.1. Dissimilar metals and their compounds possess different levels of attraction or affinity towards the electrons. When two different kinds of metals and their compounds are joined to each other through a medium called electrolyte, an electrochemical potential develops between them. Since the cathode has a lower affinity for electrons so it loses electrons and becomes positively charged whereas the anode has a higher affinity towards electrons so it becomes negatively charged [1]. Because of electrochemical potential, positive ions travel from anode to cathode via electrolyte. The main objective of electrolytes is to restrict the conduction of electrons and allows the conduction of ions through them. The neutral charge distribution gets disturbed when the ion starts traveling from anode to cathode therefore to restore it electrons start traveling through the external circuit. In the absence of an external circuit, a capacitive charge immediately accumulates to prevent the battery from discharging. To prevent the battery from short-circuiting, a separator is placed into the electrolyte region in between the cathode and anode.

Various types of electrolytes are used in Li-based batteries such as non-aqueous electrolytes, aqueous solution, ionic liquids, hybrid electrolytes, polymer electrolytes. Generally, non-aqueous solutions are used as electrolytes in commercial LIBs. In which Lithium hexafluorophosphate(LiPF₆) salt is used by dissolving it in

various types of organic carbonates such as propylene carbonate(PC) and ethyl methyl carbonate(EMC).

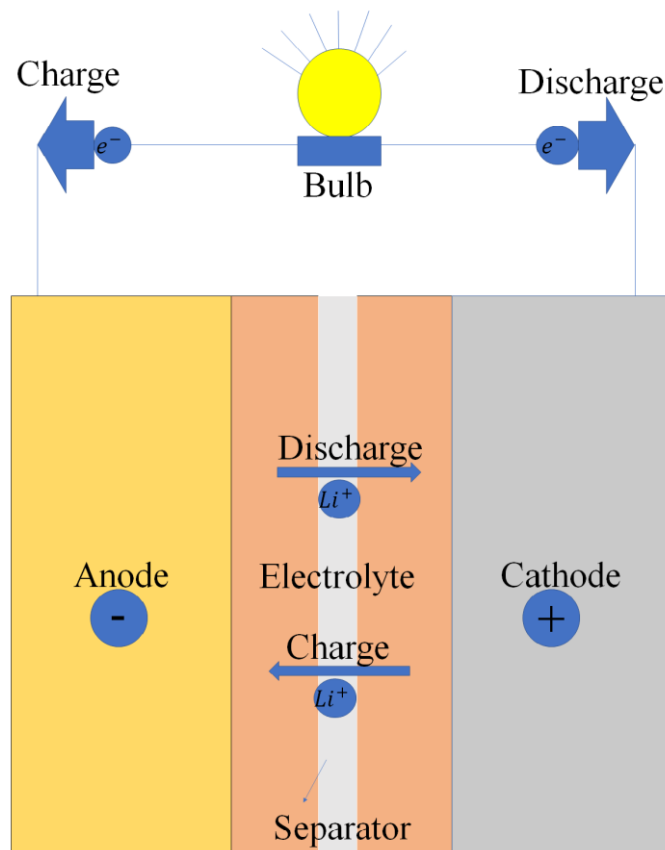


Figure 1.1 Schematic of a Li-ion battery with liquid electrolyte.

1.4 SOLID-STATE LITHIUM-ION BATTERY AND SOLID ELECTROLYTE

These are rechargeable batteries in which Li-ion is the mobile ion. During discharging Li-ions travel from the negative electrode (anode) to the positive electrode (cathode) via electrolyte and electrolyte-electrode interfaces and to maintain neutral charge distribution electrons start flowing from cathode to anode via an external circuit. While charging, the motion of both ions and electrons gets reversed [2].

Although the basic working principle of both batteries is the same. Solid-State Lithium-Ion Batteries are different from conventional batteries as the electrolyte used in these batteries are solid and it works as an electrolyte as well as a separator. Hence, electrolyte play important role in rechargeable lithium-ion batteries.

For the execution in lithium batteries, electrolytes must fulfill several preconditions [3][4][5].

1. Very low electronic conductivity.
2. High Lithium-ion conductivity.
3. Large electrochemical potential window, used for higher voltage electrodes.
4. Good chemical stability over a range of temperatures.
5. Good chemical stability for electrodes, including the fast formation of solid electrolyte interface(SEI) layer if necessary.
6. Retention of an interface(electrode-electrolyte) during the charging-discharging process.
7. Non-flammable.
8. Non-explosive.
9. Low cost.
10. Low toxicity.
11. Production(scalable) for commercialization.

Solid electrolytes fulfill several preconditions, in particular from points 1 to 8 in the inorganic solid electrolyte.

1.5 LITHIUM LANTHANUM ZIRCONIUM OXIDE ($\text{Li}_7\text{La}_3\text{Zr}_2\text{O}_{12}$)

In this study, Lithium Lanthanum Zirconium Oxide (LLZO) is chosen because of its remarkable ionic conductivity and electrochemical stability. In 2007, Murugan et al firstly reported garnet LLZO [6]. It's EIS(electrochemical impedance spectroscopy) showed that at room temperature, the ionic conductivity is of order 10^{-4} Scm^{-1} . There were other solid electrolytes such as $\text{Li}_{3x}\text{La}_{(\frac{2}{3}-x)}\text{TiO}_3$ ($0 < x < 0.16$) and $\text{Li}_{10}\text{GeP}_2\text{S}_{12}$ who have high bulk conductivity but they were failed to maintain stability when kept in contact with lithium metal [7]. LLZO exists in three phases i.e. cubic at low temperature, tetragonal and cubic at high temperature [8]. Space groups of cubic and tetragonal phases are Ia-3d [9][10] and I41/acd:2 [11] respectively. Cubic phase formed at low temperature (around 750°C , 8 hours sintering time with 30w% extra lithium salt) shows a lower ionic conductivity of about two orders in magnitude in comparison with the cubic phase formed at a higher temperature [8]. Cubic phase obtained at low

temperature is studied less because it is unstable and on raising temperature it decomposes. At lower sintering temperature (800 – 900⁰C) tetragonal structure can be obtained using the solid-state reaction method [12]. Initially, it was reported that the low-temperature cubic phase is stable which can be explained as the indirect incorporation of Al into the cubic crystal, during the high-temperature sintering process in Al₂O₃ crucibles [13][14]. Crucibles are utilized to contain the sample during the sintering process in a hot furnace. Therefore the properties of Li garnet are highly affected by the sintering and calcination process. In figure 1.2, orange, red, green, blue color depicts lithium, lanthanum, zirconium, oxygen atoms respectively of the tetragonal garnet of LLZO.

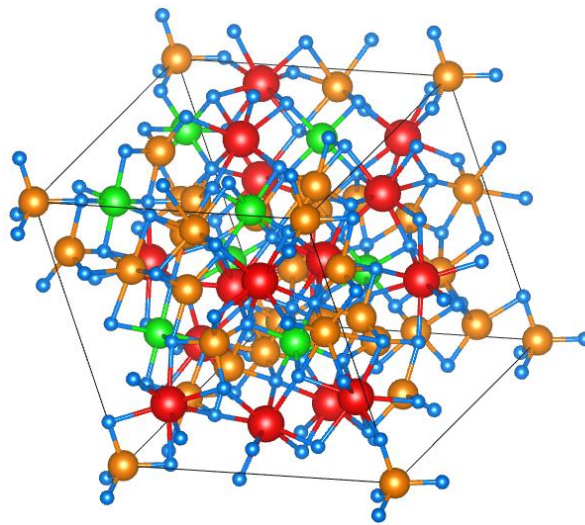


Figure 1.2 Tetragonal garnet LLZO.

Generally, the solid-state method is used to obtain LLZO because of its mass production and simple processing facilities. Sintering temperature mainly affects two properties in the LLZO i.e. relative density and lithium-ion conductivity. On raising the temperature, Li starts evaporating from the LLZO which will directly affect its lithium-ion conductivity [15][16]. With increasing sintering temperature, the relative density of solid electrolytes increases. The number of pores starts decreasing as the sintering temperature starts increasing which will lead to the higher relative density, this same thing can also be observed by SEM images of the LLZO at different sintering temperatures. One of the reasons for high ionic conductivity is the high relative density of the electrolyte material [17].

1.6 DOPING

The stability and ionic conductivity of the cubic phase of LLZO can be enhanced or modified through doping with various elements. Generally, Al and Ga are used as a dopant for enhancing stability and conductivity. On doping with Al, ionic conductivity increases because Al occupies 24d and 96h sites [9][13][19]–[22], which leads to the generation of supplementary Li vacancies in the crystal lattice. For excellent results, the concentration of Al per formula unit of solid electrolyte(LLZO) must lie between 0.15 and 0.35.

For the preparation of stable LLZO, high calcination temperature(1200 – 1300⁰C) is required, which leads to the formation of La₂Zr₂O₇ impurity. This formation of impurity decreases the Li-ion conductivity of the electrolyte. Therefore, Al₂O₃ as a sintering additive is used in the preparation of LLZO. The addition of Al₂O₃ vanishes the formation of impurity by decreasing the calcination temperature [22]. At higher sintering temperature (after 1200⁰C), a impurity called Lithium Zirconate (Li₂ZrO₃) is formed in the aluminium doped LLZO. Therefore, Ga doping is preferred over Al at a very high sintering temperature [23].

Ga doping is very useful in the formation of a stable cubic phase with higher conductivity at low sintering temperature. Because of the bigger size, instead of 24d site, Ga⁺³ occupies 96h(octahedral) site. In comparison with the 24d site, Ga⁺³ at 96h provides less hindrance for the conduction of Li-ion, which is the main reason for high conductivity on doping with Ga [24].

1.7 CHALLENGES

(a) Poor Physical Contact

Due to insufficient wetting of LLZO surface by Li metal which is used as anode in solid-state lithium-ion batteries, proper contacting of the interface between electrolyte and anode is not achieved [25]–[27]. This will lead to a higher non-uniformity of current distribution and higher resistance(interfacial) i.e nearly 10³Ω. The non-uniformity of current distribution is one of the reasons for the formation of Li metal

dendrites in LLZO during the charging-discharging process. The formation of various impurities like Li_2CO_3 and LiOH is also the reason for the poor surface wetting of LLZO. These impurities act as insulators for the movement of both electrons and lithium ions [28]–[30].

(b) Formation of lithium dendrites

Dendrite formation is due to the defects, cracks, and voids which are already present inside the solid electrolyte [28][31][32]. The work of solid electrolytes is to conduct ions and to insulate the motion of electrons through them. In comparison to perfect grains, voids and cracks have a higher tendency to diffuse electrons through them and this diffusion of electrons allows the Li dendrites to penetrate inside the solid electrolytes. Poor interfacial contact between Li metal and LLZO also helps in the dendrite formation [28][32][33].

(c) Instability in air

Impurity like Li_2CO_3 can be easily formed because of the high reactivity of LLZO with H_2O and CO_2 which is present in the air [34]. To avoid these obstacles, doping [35] and polishing of LLZO pellet plays a significant role.

1.6 OBJECTIVE OF THE RESEARCH WORK

The main objective of this research work is synthesis and various characterizations such as the structural, morphological, electrical, and dielectric properties as well as comparison of different phases of solid electrolyte LLZO sintered at same sintering temperature but at different sintering times.

CHAPTER 2

CHARACTERIZATION TECHNIQUES

2.1 X-RAY DIFFRACTION (XRD)

X-ray diffraction (XRD) is a powerful technique that is used to identify crystalline phases present in the sample material. Structural properties such as strain, phase composition, grain size, defect structure are measured using XRD. X-ray beams are incident onto the sample and get scattered by the atoms. The scattered X-rays whose angle is equal to the incident angle are received by the detector. The peak appears on the diffractogram only when the crystal is rotated properly. To obtain constructive interference of peaks on diffractometer, fulfillment of Bragg's law is necessary [36] i.e.

$$2d\sin\theta = n\lambda \quad (2.1)$$

Where n , d , λ , θ are order of diffraction, distance between imaginary atomic planes, the wavelength of the X-ray beam, and the angle between X-ray and imaginary atomic plane respectively.

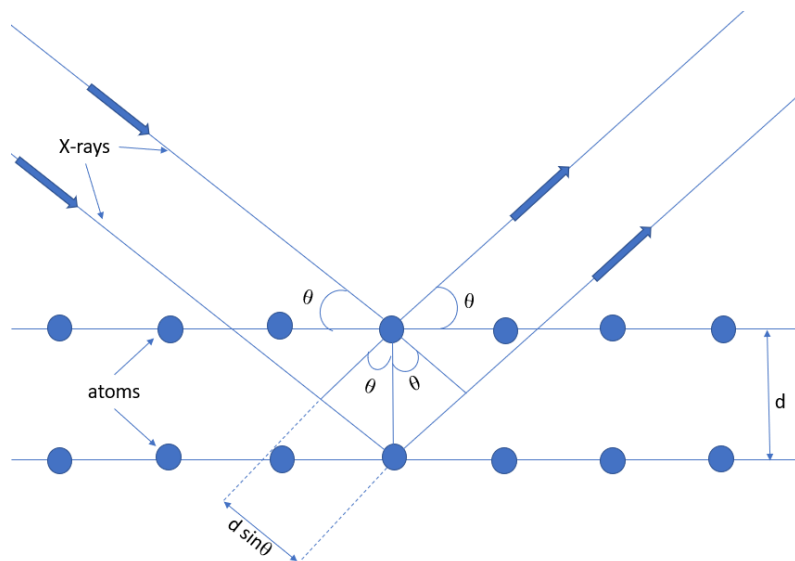


Figure 2.1 Schematic illustration of Bragg's law.

2.2 SCANNING ELECTRON MICROSCOPY (SEM)

Information related to topography and the composition near the surface regions can be investigated using scanning electron microscopy (SEM). It is an imaging technique in which electrons are incident on the specimen using a fine probe. When electrons start penetrating inside the specimen's surface, numerous interaction occurs which leads to the emission of photon and electrons from (or through) the specimen's surface. Detectors are used to collect the emitted electrons and the output of these detectors regulates the brightness of the cathode ray tube (CRT) [36].

To create a higher resolution image both secondary (SE) and backscattered electrons (BSE) are used as shown in Figure 2.2. By convention, if the energy of emitted electrons is less than 50eV then it is considered as a secondary electron. SEs are produced due to the inelastic collision of electrons of the specimen and the incoming electron beam. SE are electrons ejected from the valence shell by the electron beam. The emitted electrons whose energy is greater than 50 eV is considered BSE. BSE are electrons from the electron beam that is scattered back from the sample. The probability for emission of BSE electrons increases with an increase in atomic number. The image brightness and signal from the BSE also increases with an increase in the atomic number.

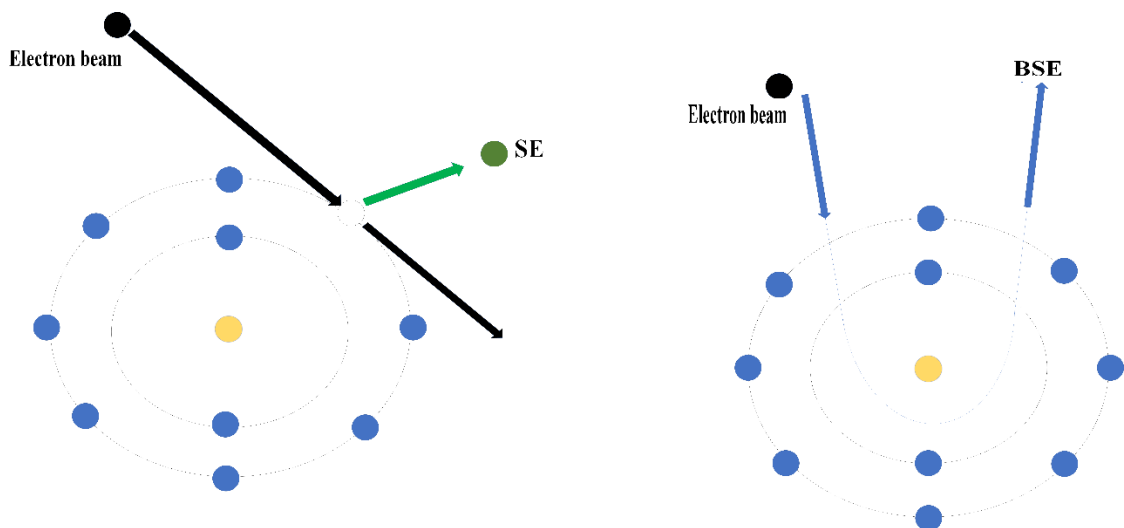


Figure 2.2 Schematic explanation of the origin of secondary electrons (SE) and backscattered electrons (BSE).

2.3 THERMAL GRAVIMETRIC ANALYSIS (TGA)

TGA is used to measure the relation of change in weight with temperature change. The obtained curve gives various information such as a change in the sample's composition, kinetic parameters for a chemical reaction in the sample. There are many more things that TGA can offer, such as:

1. Rate of reaction, Activation energy.
2. Loss of moisture, desorption, drying.
3. Estimate the lifetime of a sample (related to thermal stability).
4. Oxidation of metals in air, thermal decomposition in an inert atmosphere, oxidative decomposition of organic substance in air/O₂.
5. Effect of reactive or corrosive atmosphere on the material.

Weight loss in the sample occurs when there is a breaking of chemical bonds, loss of volatiles with raising temperature, or desorption. Whereas weight gain of sample is due to oxidation, absorption, or adsorption.

CHAPTER 3

SYNTHESIS OF TETRAGONAL (GARNET) AND MIXED-PHASE OF LLZO

3.1 INTRODUCTION

In this chapter tetragonal (garnet) and mixed-phase i.e. cubic and tetragonal garnet, are synthesized at the same sintering temperature but different sintering times through a solid-state reaction route. LLZO can be synthesized using the solution and solid-state methods such as sol-gel and solid-state reaction routes. For the solid-state reaction method, high temperature is required to overcome the lattice energy for the diffusion of anion or cation into a different site.

3.2 EXPERIMENTAL

3.2.1 Material Synthesis

Synthesis of LLZO has been carried out by the solid-state reaction route. The stoichiometric ratio of precursors of Li_2CO_3 (CDH make, purity >99%), La_2O_3 (Sigma Aldrich make, purity >99.9%), ZrO_2 (Sigma Aldrich make, purity >99%) were used for ball milling. Since at high-temperature LLZO losses lithium, to compensate for this, additional 10% Li_2CO_3 , was incorporated. All precursors were mixed via Ball Milling in an ethanol medium using steel balls. After ball milling, the powder was dried at 60 °C to remove moisture and then transferred to a furnace where it is calcined in the air atmosphere at 700 °C for 8 hrs and 10 hrs to obtain tetragonal garnet and mixed-phase respectively.

3.2.2 Material Characterization

Thermogravimetric (TGA) and Thermal differential analysis (DTA) measurements were obtained by PerkinElmer make model: TGA 4000 system. Identification of structure and phase composition of the synthesized LLZO powder has been carried by Bruker make D-8, X-Ray diffractometer in conjunction with $\text{CuK}\alpha$ as a source of radiation of wavelength, 1.54\AA . A wide scan range pattern of LLZO powder was recorded for the diffraction angle of $10\text{--}80^\circ$ with a step size of 0.02° . The morphology of the sample was examined using FEI make Nova NanoSEM 450 at an operating voltage of 15 kV.

3.3 RESULT AND DISCUSSION

3.3.1 Thermal Analysis

DTA/TG analysis is required for selecting the optimum calcination temperature to study the phase transition of the ball-milled raw material. In this work, thermal analysis curves of an as-synthesized LLZO sample are obtained by calcinating it in the air atmosphere. TGA curve shows the four-stage mass loss curve. Analysis of the TGA curve revealed that there is 0.581% weight loss in the material up to 100°C which depicts that moisture is removed from the raw material and further reacted with La_2O_3 to form $\text{La}(\text{OH})_3$ [37]. Here, two endothermic peaks are detected at 335.87°C and 446.91°C in between the temperature range of $300\text{--}500^\circ\text{C}$. The first endothermic peak can be explained by the decomposition of La_2O_3 to form intermediate compound LaOOH and H_2O is released as a byproduct [37]. Further, LaOOH reacts with CO_2 to form La_2O_3 and releases CO_2 at 446.91°C [37]. The carbonates start decomposing above 600°C [38][39]. During the transition temperature from 630°C to 750°C , there is a 4.2% weight loss in the material which reveals that Li_2CO_3 starts decomposing by releasing CO_2 and hence, it leads to the formation of LLZO. Therefore, the sample is calcinated at 700°C at different sintering times to get tetragonal garnet and intermediate phase i.e. Mixture of Tetragonal garnet and Cubic, as confirmed by XRD results.

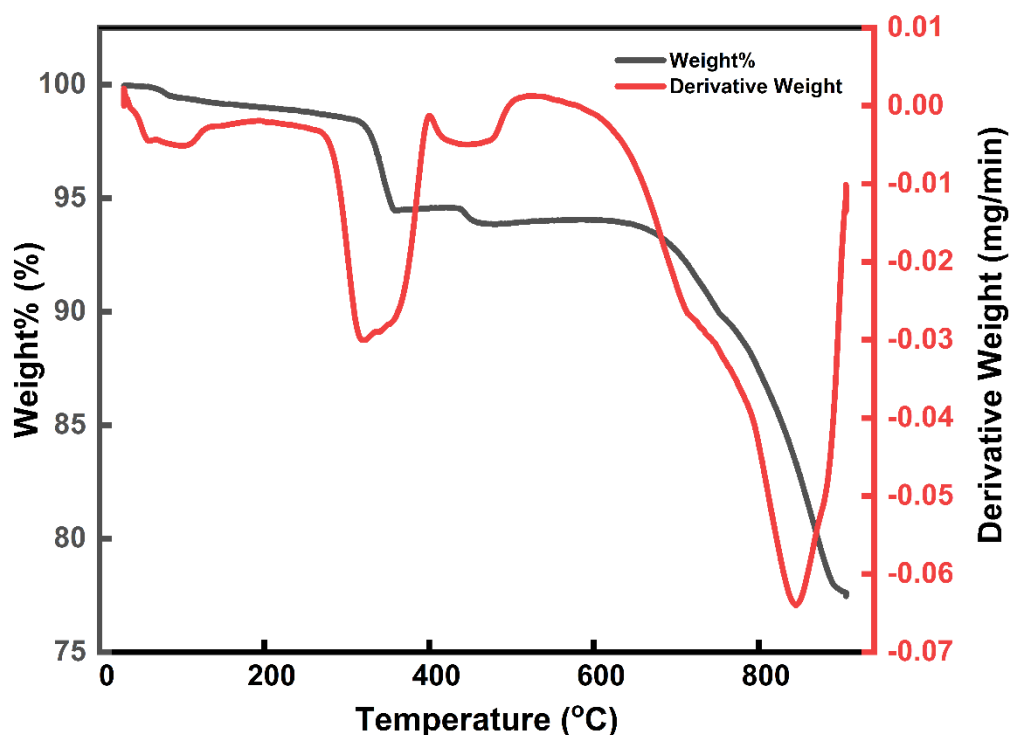


Figure 3.1 TGA and DSC curves of LLZO under air atmosphere.

3.3.2 Structural and morphological analysis

XRD analysis of as-synthesized samples of LLZO has been carried out and shown in Figure 3.2 and Figure 3.3. The XRD pattern for sintered sample at 700 °C for 10 hours is observed and it has been noticed that the observed pattern matches with the Standard XRD pattern of Cubic structure with space group, Ia-3d, (File No. 01-080-6067) and Tetragonal garnet structure of space group, I41/acd:2 (File No. 01-084-7683) as mixed phases of LLZO of (PDF- 4+2020) database. The lattice constants of tetragonal garnet and cubic structures are $a = 13.11\text{\AA}$, $b = 13.11\text{\AA}$, $c = 12.66\text{\AA}$ and $a = 13.02\text{\AA}$, $b = 13.02\text{\AA}$, $c = 13.02\text{\AA}$, respectively. Whereas the XRD pattern for LLZO sintered for 8 hours is almost identical with the Standard XRD pattern of the tetragonal garnet structure of space group, I41/acd:2 (File No.01-084-7683) of database (PDF- 4+2020). In Figure 3.2(a), the indexed peaks shown in the XRD pattern represent the existence of LLZO in two phases simultaneously (Cubic and Tetragonal garnet). In figure3.3(a), the

unknown peaks are highlighted by small green boxes. These unknown peaks can be of impurities like Li_2CO_3 and LiOH which occurs because of the instability of LLZO in air.

In Figure 3.2(b) and Figure 3.3(b), the Williamson-Hall plot is used to calculate crystallite size and microstrain from the broadening of diffraction peaks by using the following expression.

$$\beta \cos\theta = \frac{K\lambda}{D} + 4\varepsilon \sin\theta \quad (3.1)$$

Here, symbols β , ε , D , λ , and K are FWHM, micro-strain, crystallite size, wavelength of X-ray, and constant, respectively.

The intercept and slope of the linearly fitted plot between $\beta \cos\theta$ on Y-axis and $4\sin\theta$ on X-axis (figure 3.2(b) and figure 3.3(b)) give crystallite size and microstrain, respectively. Crystallite size and microstrain obtained from the plot for mixed-phase is 218nm and 2.93×10^{-4} , respectively. Whereas tetragonal garnet's crystallite size and microstrain are 95.89nm and 8.85×10^{-4} , respectively.

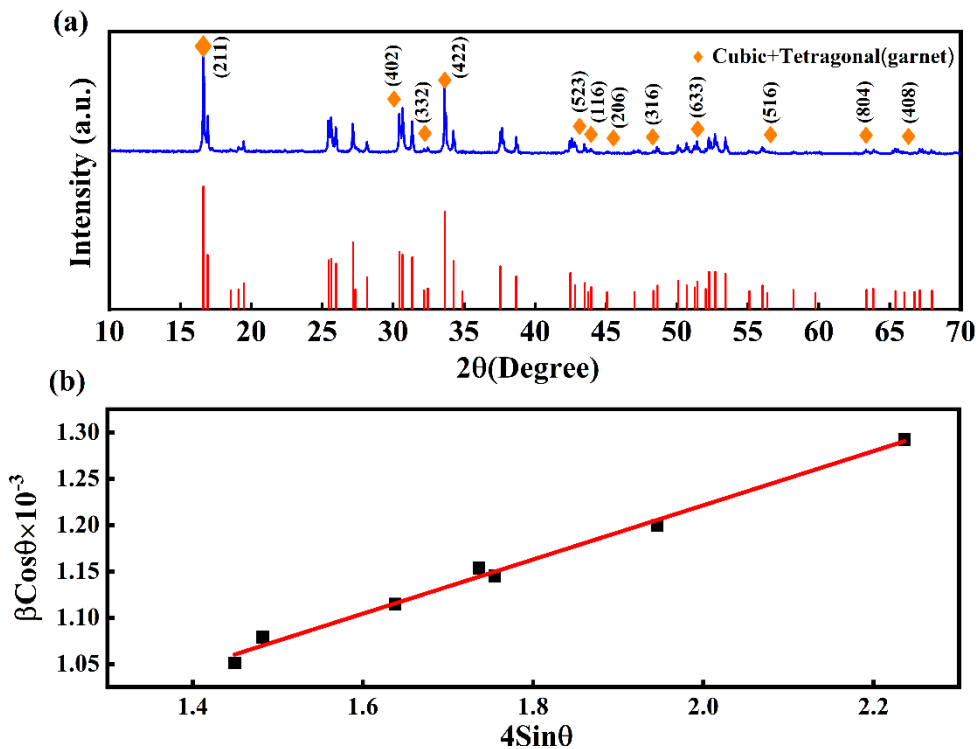


Figure 3.2. (a) XRD pattern and (b) Williamson-Hall plot of as-synthesized LLZO at calcination temperature of $700\text{ }^{\circ}\text{C}$ for 10 hours in air atmosphere.

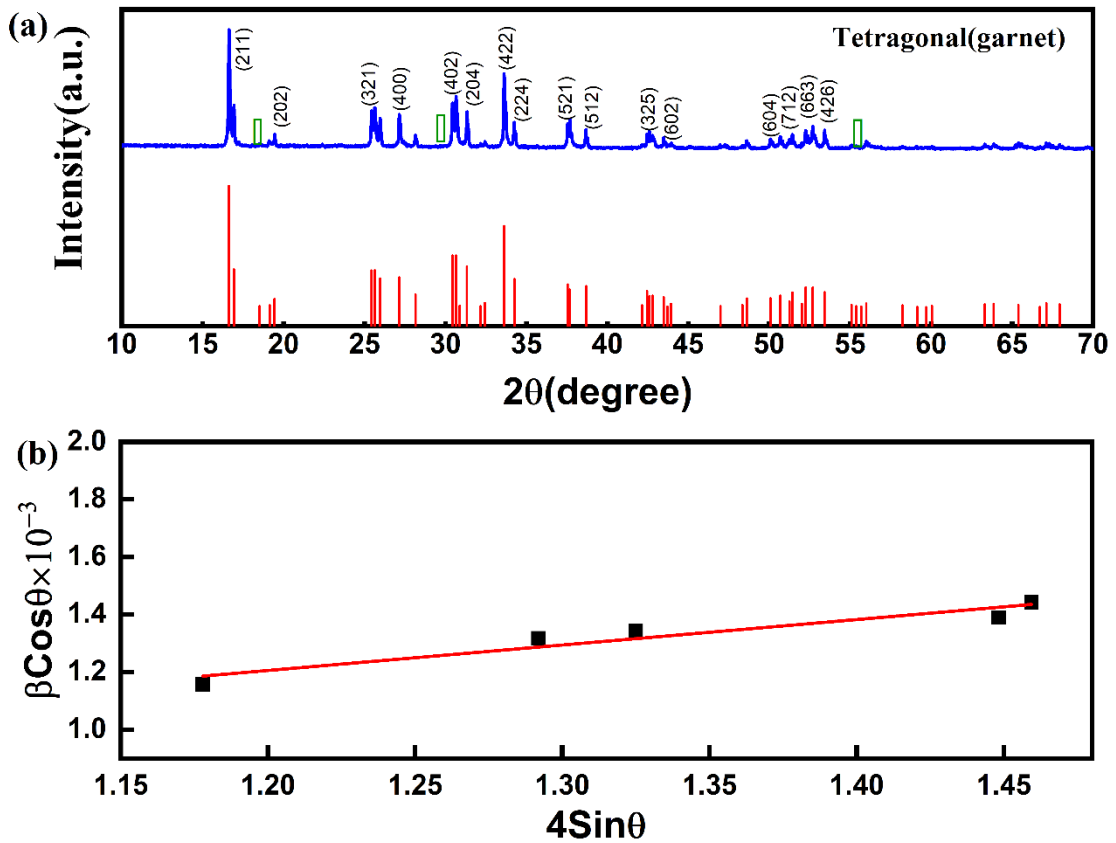


Figure 3.3. (a) XRD pattern and (b) Williamson-Hall plot of as-synthesized LLZO at calcination temperature of 700 °C for 8 hours in air atmosphere.

FESEM images of LLZO powder calcinated at 700 °C for 10 and 8 hours are shown in Figure 3.4 and figure 3.5 respectively at two magnifications of (a) 5 μm and (b) 400nm. The size of particles is directly influenced by the calcination temperature. Figure 3.4(a) shows that particles are dense and partially agglomerated with irregular morphology in this intermediate stage of LLZO. This agglomeration is due to the alteration of one phase to another i.e. Cubic to Tetragonal (garnet), which results in the declination of bulk ionic conductivity of the material. On further magnifying the features observed in the micrograph of Figure 3.4 (a), a dense layered (staircase-like) morphology is observed at the nano level (Figure 3.4 (b)). Whereas on magnifying the FESEM image of tetragonal garnet, a sheet-like porous structure is observed as shown in figure 3.5 (b).

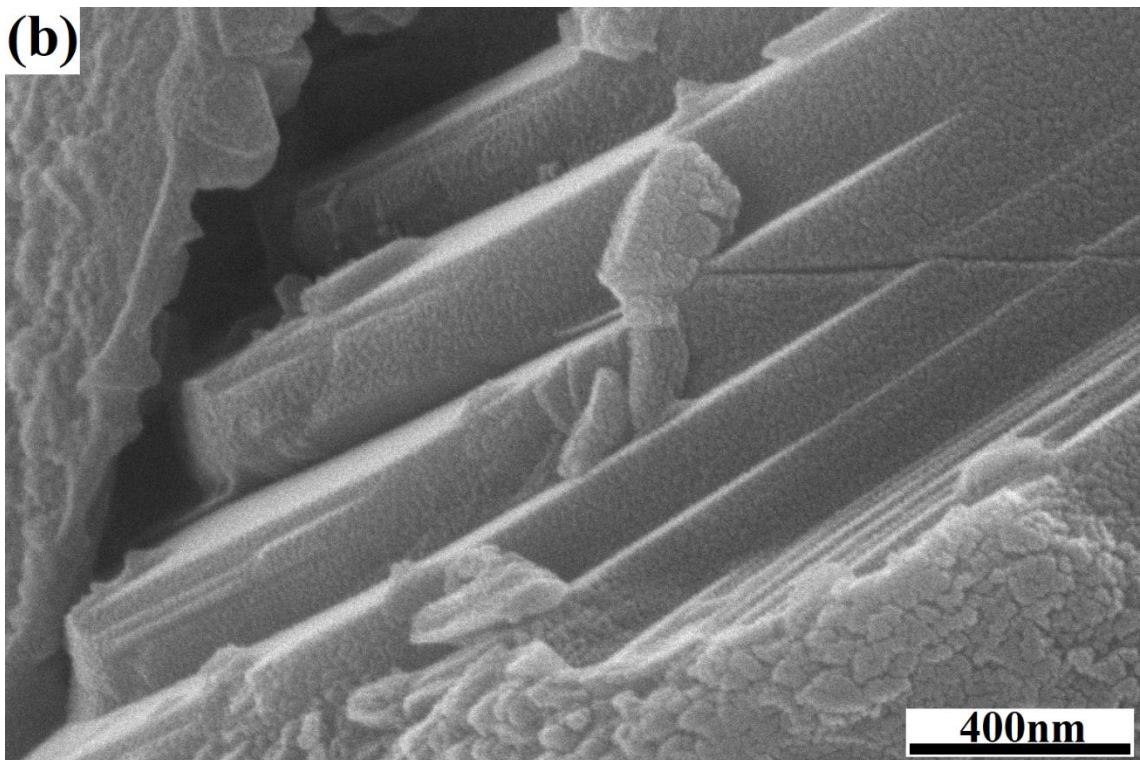
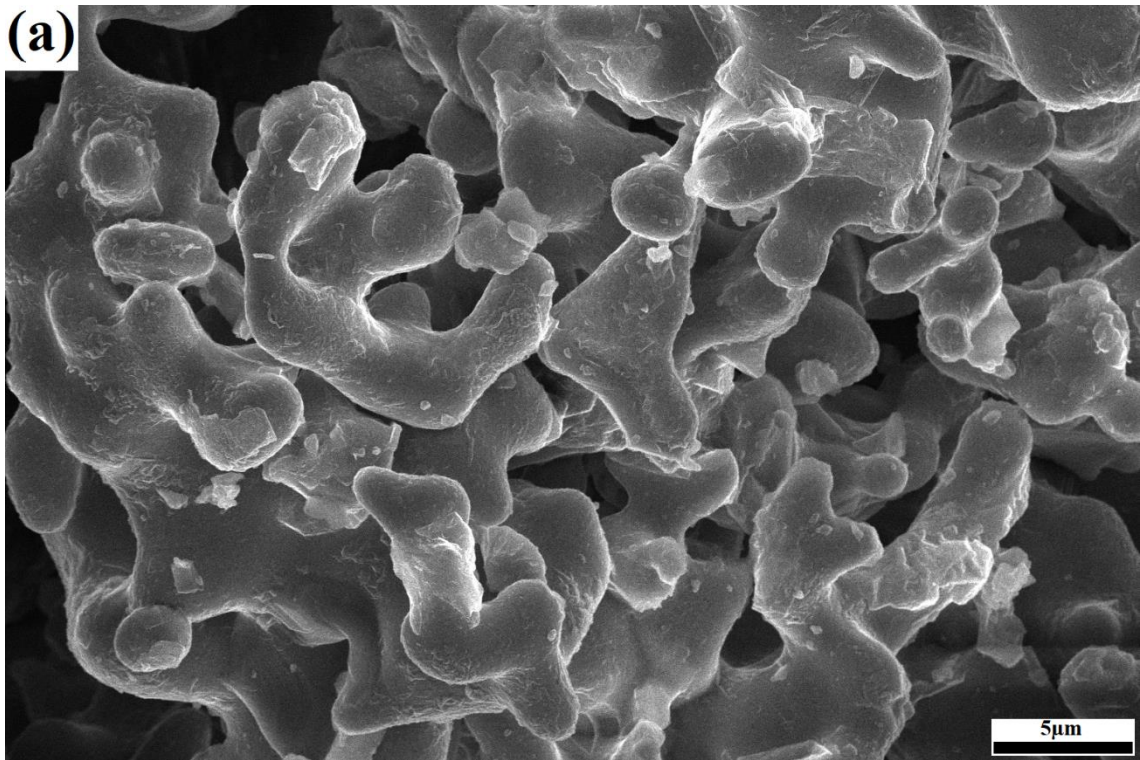


Figure 3.4. SEM image of mixed-phase of LLZO, sintered for 10 hours (a)5μm
(b)400nm.

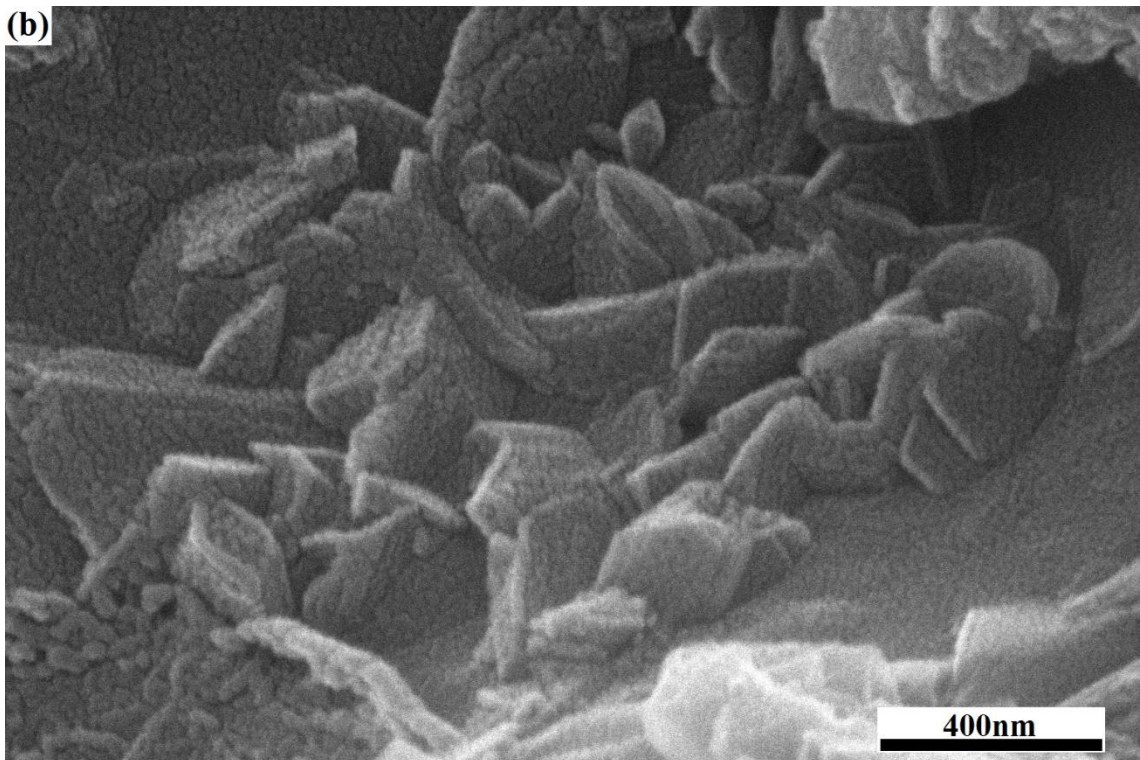
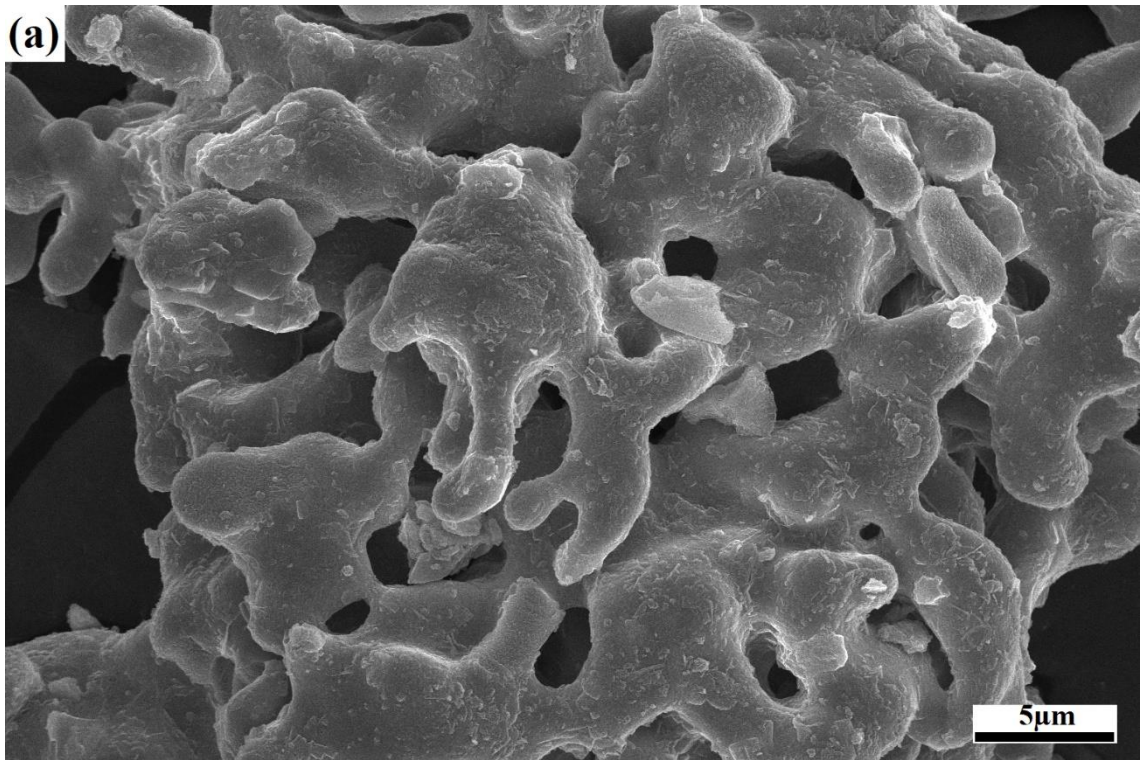


Figure 3.5. SEM image of tetragonal garnet of LLZO, sintered for 8 hours (a)5μm
(b)400nm.

CHAPTER 4

STUDY OF ELECTRICAL AND DIELECTRIC PROPERTIES OF MIXED AND TETRAGONAL GARNET PHASE OF LLZO

4.1 INTRODUCTION

The objective of this chapter is to present the work on the electrical and dielectric properties of mixed and tetragonal (garnet) phases of LLZO. The impact of higher frequencies above 70 kHz on the conductivity, dielectric constant, and dielectric loss is discussed. Explanation regarding the conduction mechanism and the interfacial polarization is briefly described. Further comparison in electric and dielectric properties of both the phases is also shown. Arrhenius behavior of both the phases is compared and used to calculate their respective activation energy.

4.2 EXPERIMENTAL

4.2.1 Pellet Formation and polishing

After the sintering process powder was allowed to come to room temperature and then grind by using a pestle and mortar for 30 minutes. The obtained fine powder was pressed in the hydraulic machine to make pellets of diameter 10 mm at a pressure of 60 MPa. These pellets were then dried at 80 °C temperature for 30 minutes to remove any remaining moisture. Further, both the surfaces of the Pellets were polished with Silver paste to make them conductive. After polishing, the pellets were again dried at 80 °C temperature for 30 minutes.

4.2.2 Material Characterization

AC impedance spectroscopy of LLZO pellets was obtained by HIOKI make 3532 LCR oscilloscope in the high-frequency range of 72 kHz to 5 MHz within the temperature range 30 °C and 100 °C to record four parameters such as R_p (Parallel resistance), C_p (Parallel capacitance), D (Dissipation factor), and Z (Total Impedance). Complex Impedance (Z^*), Real part (Z'), and Imaginary part (Z'') of Impedance are related to each other as $Z^* = Z' + jZ''$. Here Z'' and Z' can be determined using the following equations.

$$Z'' = \frac{2\pi R_p^2 C_p f}{1 + R_p^2 C_p^2 4\pi^2 f^2} \quad (4.1)$$

$$Z' = \frac{R_p}{1 + R_p^2 C_p^2 4\pi^2 f^2} \quad (4.2)$$

Other frequency related properties of LLZO can be explained by the Complex Dielectric Constant (ϵ^*), Dielectric Constant (ϵ'), Dielectric Loss (ϵ'') and Dissipation factor ($\tan\delta$). These parameters are related to each other as $\epsilon^* = \epsilon' + j\epsilon''$. The real part of the complex dielectric was calculated from.

$$\epsilon' = \frac{C_p d}{A\epsilon_0} \quad (4.3)$$

Where C_p = Parallel capacitance, d = thickness of pellet, A = Area of pellet, ϵ_0 = permittivity of free space.

$$\tan\delta = \frac{\epsilon''}{\epsilon'} \quad (4.3)$$

Further, A.C. conductivity is calculated using the given relation:

$$\sigma_{a.c.} = \omega\epsilon_0\epsilon'' \quad (4.4)$$

4.3 RESULT AND DISCUSSION

4.3.1 Electrical Measurement

Dependency of AC conductivity, $\sigma_{a.c}$ on frequency and temperature of both the phases is shown in Figure 4.1(a) and (b) at logarithmic scale as $\log\sigma_{a.c}$ vs $\log\omega$ for different temperatures from 30 °C to 100 °C for as-synthesized LLZO. The A.C. conductivity increases with an increase in temperature. These curves at various temperatures show two regions. Initially, at low frequency the logarithmic value of a.c. conductivity remains nearly constant. In comparison with mixed phase, tetragonal (garnet) has higher a.c. conductivity. In the high-frequency region, the logarithmic value shows linear dependency on the frequency. Nature of graph can be characterized by using Universal Dynamic Response Equation (the power law, Eq.4.5 [40]) given as:

$$\sigma_{a.c} = A\omega^n \quad (4.5)$$

Where the constant A represents the strength of polarization and n is the frequency exponent. The slope and intercept of $\log\sigma_{a.c}$ vs $\log\omega$ plot represent the frequency exponent and the constant A at the corresponding temperature respectively. Therefore n can be written as:

$$n = \frac{\Delta \ln \sigma_{a.c.}}{\Delta \ln \omega} \quad (4.6)$$

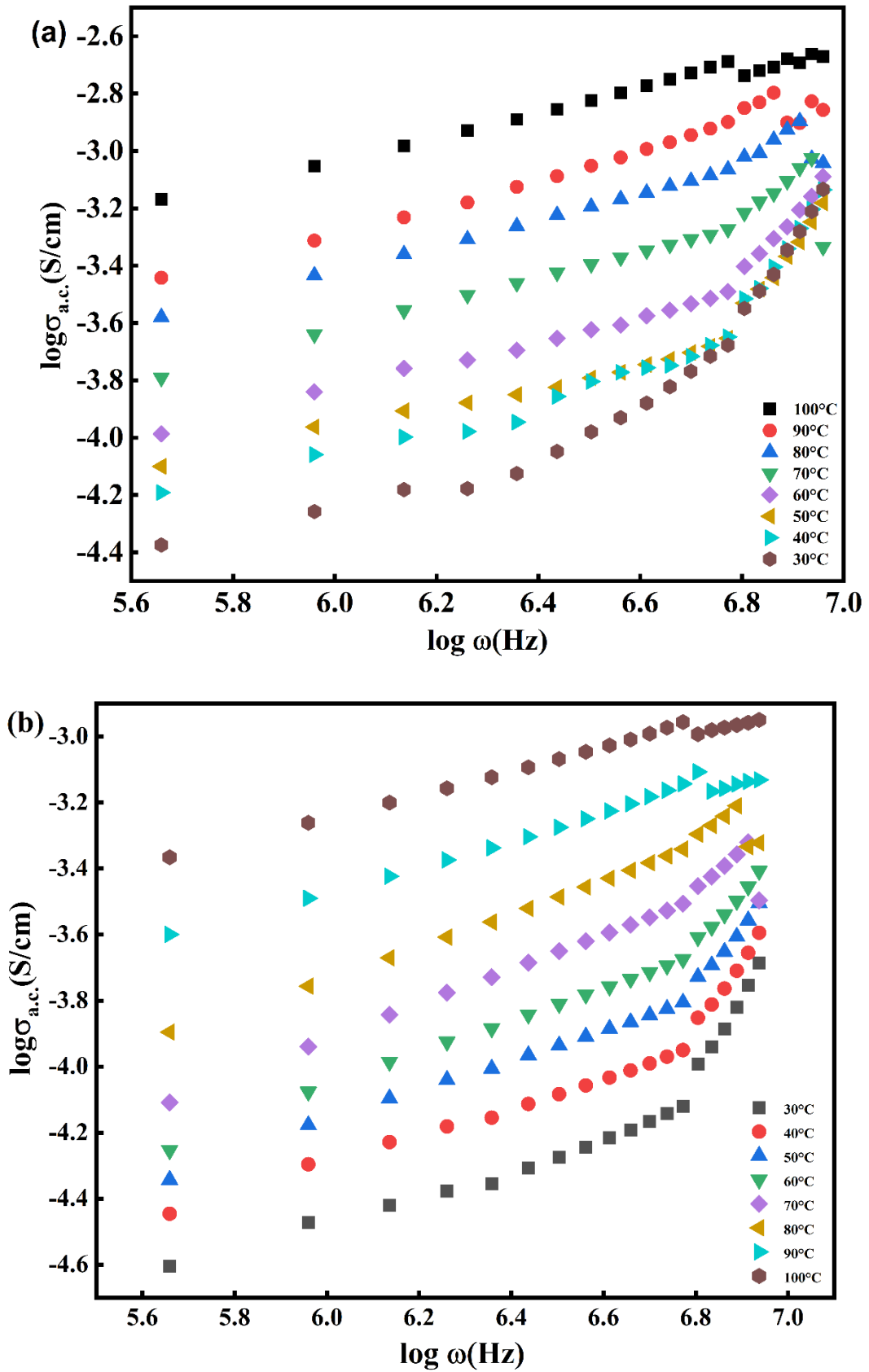


Figure 4.1 AC conductivity versus the frequency at the temperature range of 30 °C to 100 °C, (a) mixed-phase (b) tetragonal(garnet) of LLZO.

Table 4.1. The calculated value of n and A of mixed-phase at different temperatures.

Temperature(K)	n	A[S/(cm.rad.s)]
303	0.99922	0.000032599
313	0.72772	0.000208945
323	0.587	0.000534826
333	0.57689	0.000658695
343	0.47874	0.00150669
353	0.45657	0.002116482
363	0.44742	0.002550591
373	0.386	0.00478648

Table 4.2. The calculated value of n and A of tetragonal(garnet) at different temperatures.

Temperature(K)	n	A[S/(cm.rad.s)]
303	0.65627	0.00021178266
313	0.59896	0.0003624116
323	0.5924	0.0004307856
333	0.56394	0.0005758922
343	0.55383	0.0007131848
353	0.51197	0.00110584
363	0.38653	0.0030645026
373	0.32974	0.005408735

Three different phenomena are used to explain the conduction mechanism [41] such as Classical hopping over the barrier, Quantum mechanical tunneling (QMT), and small polaron tunneling.

In the QMT model, the expression of n is given by:

$$n = 1 - \frac{4}{\ln \frac{v_{ph}}{\omega}} \quad (4.7)$$

While for small polaron [42]:

$$n = 1 - \frac{4}{\ln \frac{1}{\omega\tau} - \frac{W_H}{kT}} \quad (4.8)$$

And for classical hopping:

$$n = 1 - \frac{6kT}{E_0 - kT \ln \frac{v_{ph}}{\omega}} = 1 - \frac{6kT}{E_0 - kT \ln \frac{1}{\omega\tau}} \quad (4.9)$$

It is clear from Eq.4.7 and Eq.4.8 that n is independent of temperature for the QMT model and increases with temperature for small polaron tunneling. Table 1 and Table 2 shows that n is decreasing with an increase in the temperature which points out that the conduction mechanism in the mixed and tetragonal(garnet) phases of LLZO is majorly due to Classical hopping.

The activation energy at frequency, 70kHz is calculated from the Arrhenius plot shown in Figure 4.2. The activation energy for the mixed and tetragonal(garnet) phases of LLZO are observed as 0.1605 eV and 0.16506 eV respectively.

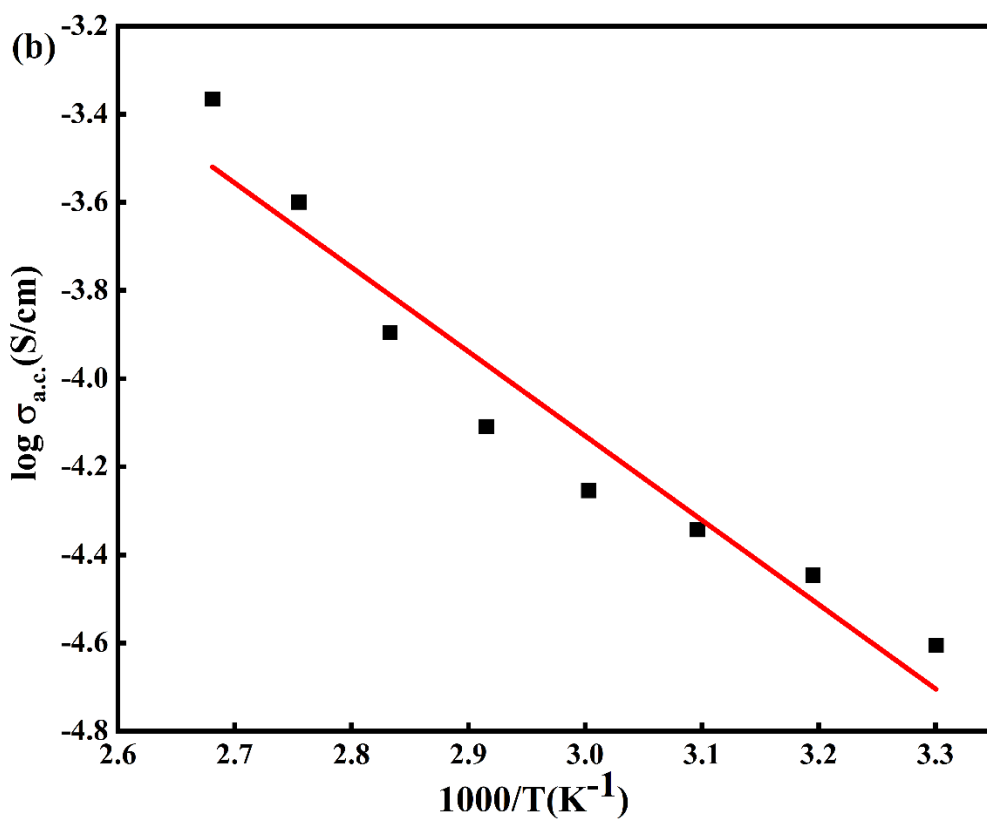
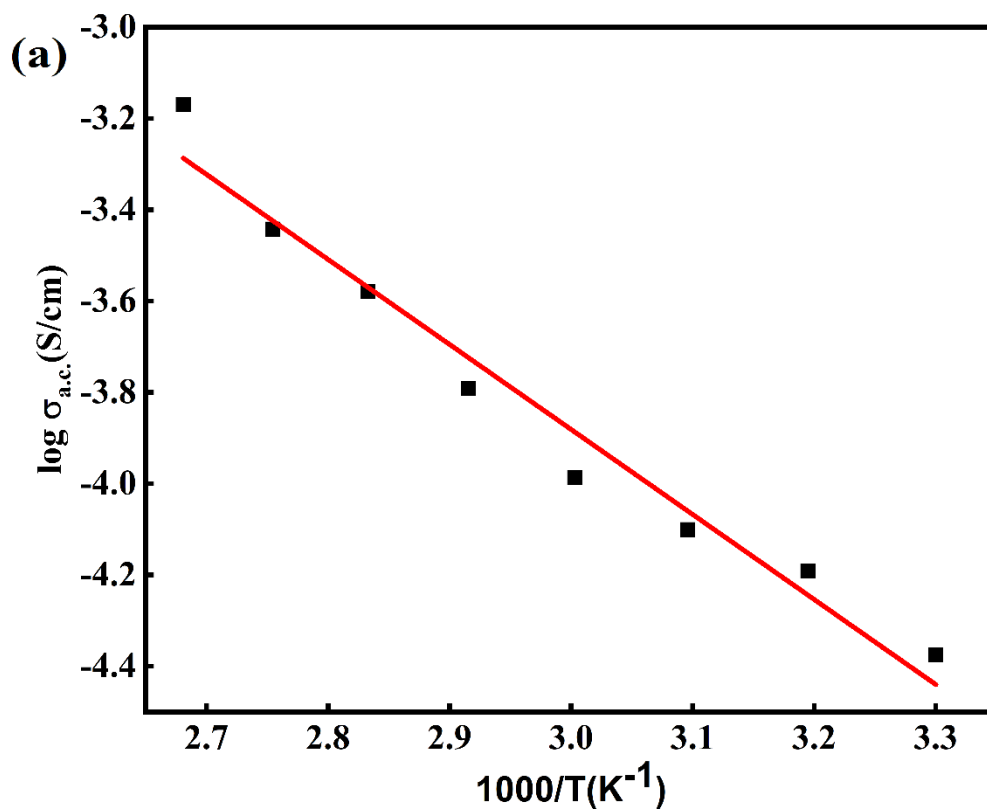


Figure 4.2 Arrhenius plot, variation of conductivity with temperature for as-synthesized LLZO, (a) mixed-phase (b) tetragonal(garnet)

4.3.2 Dielectric Measurement

The calculated values of constant A for both the mixed and tetragonal(garnet) phases of LLZO are shown in Table 4.1 and Table 4.2 respectively. In both phases, the value of A increases with an increase in the temperature which signifies that polarizability increases with increasing temperature. In comparison with mixed-phase, tetragonal(garnet) has higher values of A which depicts that it is more affected by the external electric field and leads to a higher value of the strength of polarisation. This dependency has also been confirmed by the dielectric constant as shown in Figure 4.3 (a) and (b). It clearly shows the behavior of the dielectric constant (ϵ') with frequency and temperature. ϵ' is gradually decreasing with increasing frequency which shows dielectric dispersive behavior of both the phases of LLZO at higher frequencies [43]. This dielectric dispersion phenomenon is also confirming the classical charge hopping mechanism. The higher value of ϵ' at low frequency can be explained by space charge polarisation in which polarization and migration of Li^+ takes place [43] and the existing dipoles in the material orient themselves in the field change. At higher frequencies, ϵ' become nearly constant which can be explained as the inability of the electric dipole to adapt themselves to varying external electric fields. On increasing temperature dielectric constant also increases due to the alignment of dipoles along the electric field direction. On applying an electric field across the material, ionic motion starts through classical hopping. Since grain boundaries offer a significant amount of resistance therefore at grain boundaries electrons get stacked up [44] which induces polarization at grain boundaries (Interfacial Maxwell Wagner polarization) [45]. ϵ'' and ϵ' shows a similar type of behavior with frequency. Figure 4.4 (a) and (b) indicates that ϵ'' first decreases with frequency and becomes nearly constant at a higher value of frequency. Since a certain amount of electrical energy is absorbed by the dipolar molecules of the material for orienting themselves along the applied field leads to dielectric loss. The increase in ϵ'' with increasing temperature shows the thermal dependence of dielectric relaxation of the material.

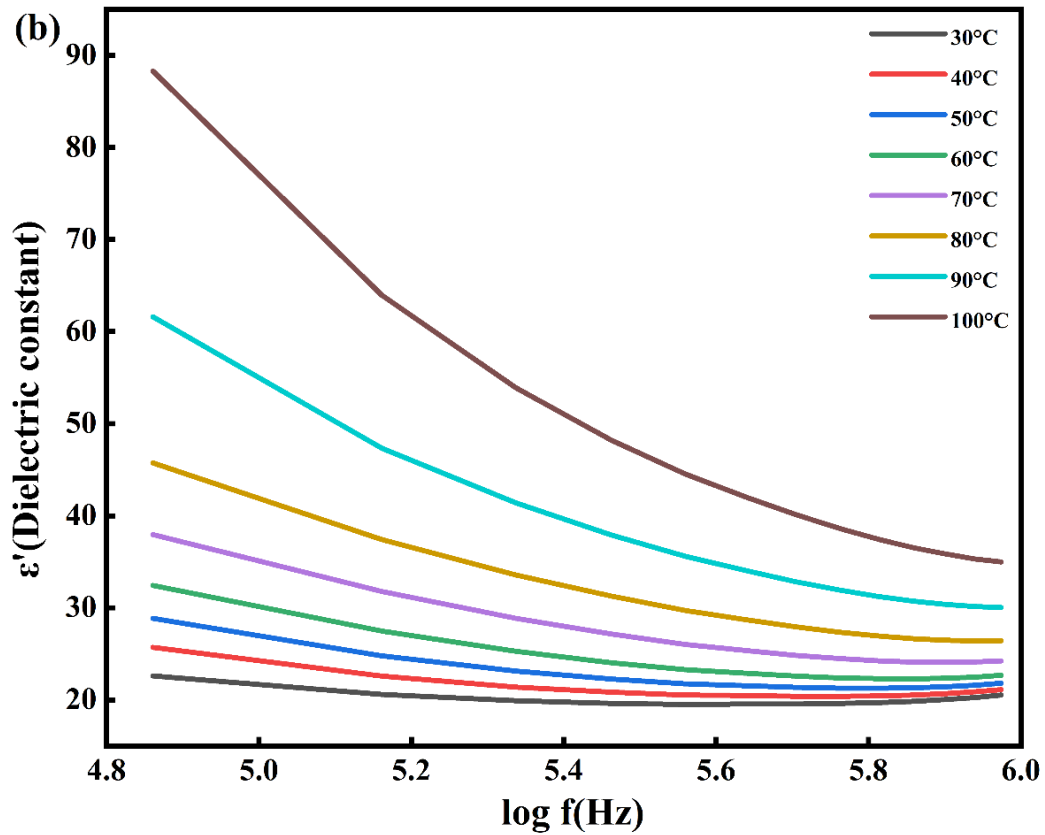
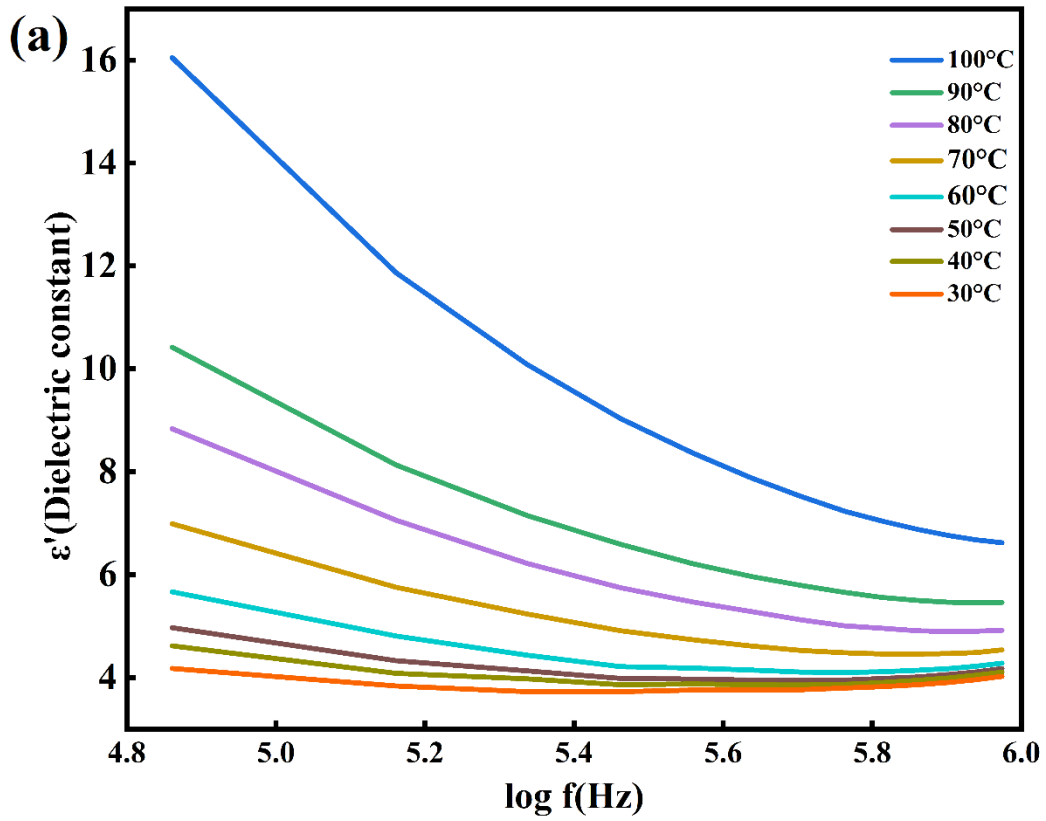


Figure 4.3. Dielectric constant versus the logarithm of frequency at various temperatures, (a) mixed-phase (b) tetragonal garnet.

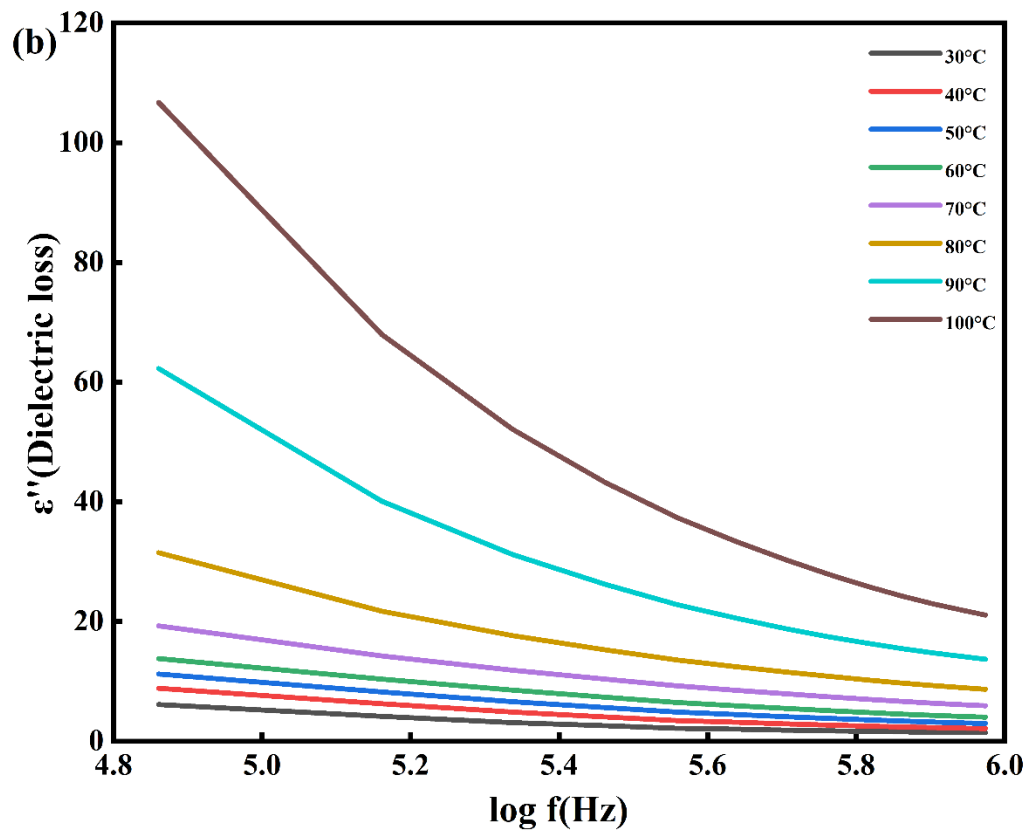
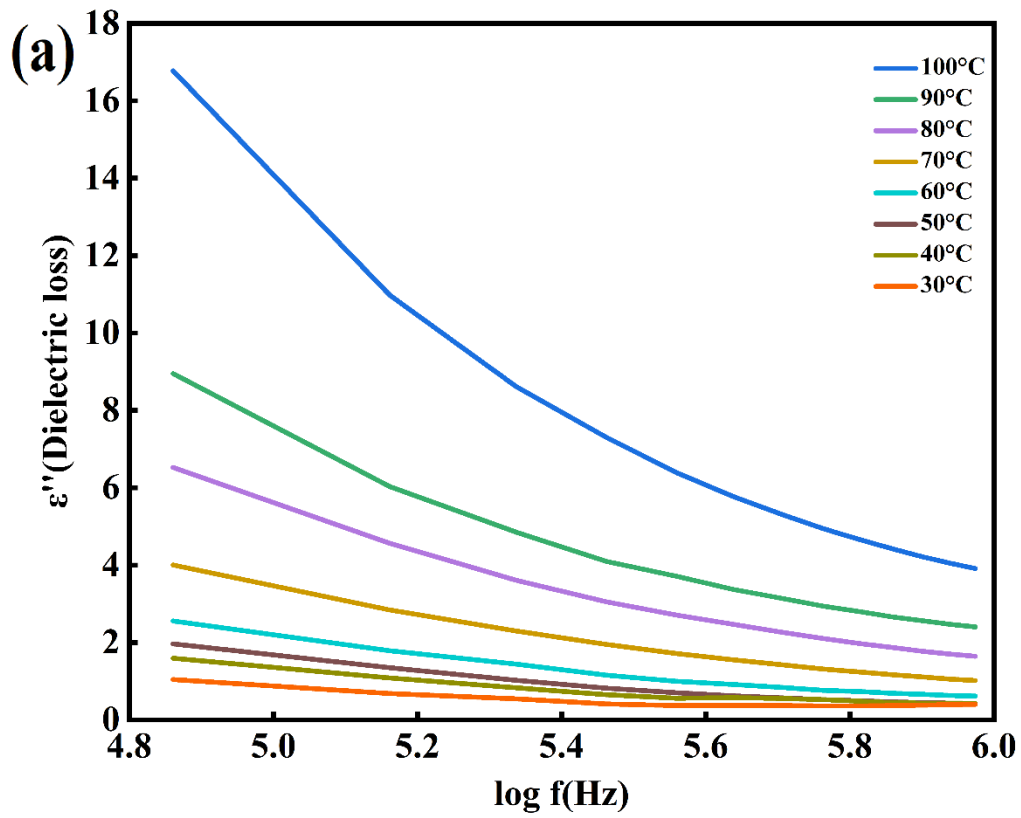


Figure 4.4. Dielectric loss versus the logarithm of frequency at various temperatures, (a) mixed-phase (b) tetragonal garnet.

CHAPTER 5

CONCLUSION AND FUTURE WORK

CONCLUSION

Mixed and tetragonal garnet phases of $\text{Li}_7\text{La}_3\text{Zr}_2\text{O}_{12}$ (LLZO) have been successfully synthesized using a solid-state reaction route at low sintering temperature by changing sintering time. DTA/TGA results confirms that the LLZO phase is formed at 700°C . XRD results reveal the formation of a mixed-phase (tetragonal garnet and cubic) and tetragonal garnet phase of LLZO for 10 and 8 hours of sintering time. From the Williamson-Hall method, an average crystallite size of mixed-phase is 218nm, and a strain of 2.93×10^{-4} are obtained. Whereas for tetragonal garnet average crystallite size and strain are 95.89nm and 8.85×10^{-4} , respectively. FESEM images show that particles of mixed-phase are partially agglomerated and have a dense layered (staircase-like) structure and particles of tetragonal garnet have a sheet-like porous structure at the nano level. The obtained LLZO samples were used for electrical analysis. The A.C. conductivity of both LLZO phases shows a significant dependence on the frequency which can be correlated by UDR. In the temperature region of 303K to 373K for both phases, the frequency exponent of the power-law equation confirms that the conduction mechanism is taking place through Classical Hopping and the activation energy at 70kHz is 0.16eV. The dielectric analysis shows that variation of dielectric properties can be explained by space charge polarization i.e. hopping polarization and interfacial polarization (Maxwell Wagner polarization).

The present studies show that mixed-phase and tetragonal garnet LLZO is synthesized at low temperature by varying sintering time and their structural, morphological, dielectric, and electric properties were successfully studied.

FUTURE WORK

In continuation of our work, we will try to synthesize cubic garnet phase LLZO at low temperatures with enhanced properties so that it can provide a wide electrochemical window to commercial cathodes.

REFERENCES

- [1] N. Chawla, N. Bharti, and S. Singh, “Recent advances in non-flammable electrolytes for safer lithium-ion batteries,” *Batteries*, vol. 5, no. 1. MDPI Multidisciplinary Digital Publishing Institute, p. 19, Mar. 01, 2019, doi: 10.3390/batteries5010019.
- [2] F. Zheng, M. Kotobuki, S. Song, M. Lai, L. L.-J. of P. Sources, and undefined 2018, “Review on solid electrolytes for all-solid-state lithium-ion batteries,” *Elsevier*.
- [3] J. B. Goodenough and Y. Kim, “Challenges for rechargeable Li batteries,” *Chemistry of Materials*, vol. 22, no. 3. pp. 587–603, Feb. 09, 2010, doi: 10.1021/cm901452z.
- [4] P. Knauth, “Inorganic solid Li ion conductors: An overview,” *Solid State Ionics*, vol. 180, no. 14–16. pp. 911–916, Jun. 25, 2009, doi: 10.1016/j.ssi.2009.03.022.
- [5] M. Balaish, A. Kraytsberg, and Y. Ein-Eli, “Article in Physical Chemistry Chemical Physics,” *Phys. Chem. Chem. Phys*, vol. 16, no. 7, p. 2801, Feb. 2014, doi: 10.1039/c3cp54165g.
- [6] H. Xie, Y. Li, and J. B. Goodenough, “Low-temperature synthesis of $\text{Li}_7\text{La}_3\text{Zr}_2\text{O}_{12}$ with cubic garnet-type structure,” *Mater. Res. Bull.*, vol. 47, no. 5, pp. 1229–1232, 2012, doi: 10.1016/j.materresbull.2012.01.027.
- [7] Y. Inaguma *et al.*, “High ionic conductivity in lithium lanthanum titanate,” *Solid State Commun.*, vol. 86, no. 10, pp. 689–693, 1993, doi: 10.1016/0038-1098(93)90841-A.
- [8] H. Xie, Y. Li, J. G.-M. R. Bulletin, and undefined 2012, “Low-temperature synthesis of $\text{Li}_7\text{La}_3\text{Zr}_2\text{O}_{12}$ with cubic garnet-type structure,” *Elsevier*.

- [9] J. Awaka, A. Takashima, K. Kataoka, N. Kijima, Y. Idemoto, and J. Akimoto, “Crystal structure of fast lithium-ion-conducting cubic $\text{Li}_7\text{La}_3\text{Zr}_2\text{O}_{12}$,” *Chem. Lett.*, vol. 40, no. 1, pp. 60–62, 2011, doi: 10.1246/cl.2011.60.
- [10] A. Kim, S. Woo, M. Kang, H. Park, B. K.-F. in Chemistry, and undefined 2020, “Research progresses of garnet-type solid electrolytes for developing all-solid-state Li batteries,” *ncbi.nlm.nih.gov*.
- [11] J. Awaka, N. Kijima, H. Hayakawa, and J. Akimoto, “Synthesis and structure analysis of tetragonal $\text{Li}_7\text{La}_3\text{Zr}_2\text{O}_{12}$ with the garnet-related type structure,” *J. Solid State Chem.*, vol. 182, no. 8, pp. 2046–2052, Aug. 2009, doi: 10.1016/j.jssc.2009.05.020.
- [12] W. Xue *et al.*, “The effect of sintering process on lithium ionic conductivity of $\text{Li}_{6.4}\text{Al}_{0.2}\text{La}_3\text{Zr}_2\text{O}_{12}$ garnet produced by solid-state synthesis,” *pubs.rsc.org*.
- [13] H. Buschmann *et al.*, “Structure and dynamics of the fast lithium ion conductor ‘ $\text{Li}_7\text{La}_3\text{Zr}_2\text{O}_{12}$,’” *Phys. Chem. Chem. Phys.*, vol. 13, no. 43, pp. 19378–19392, Nov. 2011, doi: 10.1039/c1cp22108f.
- [14] E. Rangasamy, J. Wolfenstine, and J. Sakamoto, “The role of Al and Li concentration on the formation of cubic garnet solid electrolyte of nominal composition $\text{Li}_7\text{La}_3\text{Zr}_2\text{O}_{12}$,” *Solid State Ionics*, vol. 206, pp. 28–32, Jan. 2012, doi: 10.1016/j.ssi.2011.10.022.
- [15] R. Chen, M. Huang, W. Huang, Y. Shen, Y. L.-S. S. Ionics, and undefined 2014, “Effect of calcining and Al doping on structure and conductivity of $\text{Li}_7\text{La}_3\text{Zr}_2\text{O}_{12}$,” *Elsevier*.
- [16] E. Rangasamy, J. Wolfenstine, J. S.-S. S. Ionics, and undefined 2012, “The role of Al and Li concentration on the formation of cubic garnet solid electrolyte of nominal composition $\text{Li}_7\text{La}_3\text{Zr}_2\text{O}_{12}$,”
- [17] Y. Kim, H. Jo, J. L. Allen, H. Choe, J. Wolfenstine, and J. Sakamoto, “The Effect

- of Relative Density on the Mechanical Properties of Hot-Pressed Cubic $\text{Li}_7\text{La}_3\text{Zr}_2\text{O}_{12}$,” *J. Am. Ceram. Soc.*, vol. 99, no. 4, pp. 1367–1374, Apr. 2016, doi: 10.1111/jace.14084.
- [18] C. Chemistry *et al.*, “Garnet: A Fast Lithium-Ion Conductor,” *Inorg. Chem*, vol. 50, no. 3, p. 1089, Feb. 2011, doi: 10.1021/ic101914e.
- [19] H. Buschmann *et al.*, “19378-Cite this,” *Phys. Chem. Chem. Phys*, vol. 13, no. 43, pp. 19378–19392, Nov. 2011, doi: 10.1039/c1cp22108f.
- [20] J. Lamb, C. Orendorff, L. S.-J. of P. Sources, and undefined 2015, “Failure propagation in multi-cell lithium ion batteries,” *Elsevier*.
- [21] S. Ohta, T. Kobayashi, and T. Asaoka, “High lithium ionic conductivity in the garnet-type oxide $\text{Li}_{7-X}\text{La}_3(\text{Zr}_{2-X}\text{Nb}_X)\text{O}_{12}$ ($X = 0-2$),” *J. Power Sources*, vol. 196, no. 6, pp. 3342–3345, Mar. 2011, doi: 10.1016/j.jpowsour.2010.11.089.
- [22] M. Kotobuki, K. Kanamura, Y. Sato, T. Y.-J. of P. Sources, and undefined 2011, “Fabrication of all-solid-state lithium battery with lithium metal anode using Al_2O_3 -added $\text{Li}_7\text{La}_3\text{Zr}_2\text{O}_{12}$ solid electrolyte,” *Elsevier*.
- [23] M. Mishra *et al.*, “Ga-doped lithium lanthanum zirconium oxide electrolyte for solid-state Li batteries,” *Electrochim. Acta*, vol. 353, Sep. 2020, doi: 10.1016/j.electacta.2020.136536.
- [24] J. Allen, J. Wolfenstine, ... E. R.-J. of P., and undefined 2012, “Effect of substitution (Ta, Al, Ga) on the conductivity of $\text{Li}_7\text{La}_3\text{Zr}_2\text{O}_{12}$,” *Elsevier*,
- [25] M. Kotobuki, H. Munakata, K. Kanamura, Y. Sato, and T. Yoshida, “Compatibility of $\text{Li}_{7-x}\text{La}_3\text{Zr}_2\text{O}_{12}$ Solid Electrolyte to All-Solid-State Battery Using Li Metal Anode,” *J. Electrochem. Soc.*, vol. 157, no. 10, p. A1076, 2010, doi: 10.1149/1.3474232.
- [26] H. Buschmann *et al.*, “19378-Cite this,” *Phys. Chem. Chem. Phys*, vol. 13, no. 43, pp. 19378–19392, Nov. 2011, doi: 10.1039/c1cp22108f.

- [27] K. Fu, Y. Gong, B. Liu, Y. Zhu, ... S. X.-S., and undefined 2017, "A P P L I E D S C I E N C E S A N D E N G I N E E R I N G," 2017.
- [28] L. Cheng *et al.*, "Effect of Surface Microstructure on Electrochemical Performance of Garnet Solid Electrolytes," *ACS Publ.*, vol. 7, no. 3, pp. 2073–2081, Jan. 2015, doi: 10.1021/am508111r.
- [29] W. Xia *et al.*, "Ionic Conductivity and Air Stability of Al-Doped Li₇La₃Zr₂O₁₂ Sintered in Alumina and Pt Crucibles," *ACS Appl. Mater. Interfaces*, vol. 8, no. 8, pp. 5335–5342, Mar. 2016, doi: 10.1021/acsami.5b12186.
- [30] A. Sharafi *et al.*, "Surface Chemistry Mechanism of Ultra-Low Interfacial Resistance in the Solid-State Electrolyte Li₇La₃Zr₂O₁₂," *Chem. Mater.*, vol. 29, no. 18, pp. 7961–7968, Sep. 2017, doi: 10.1021/acs.chemmater.7b03002.
- [31] K. Kerman, A. Luntz, ... V. V.-J. of T., and undefined 2017, "Review-Practical Challenges Hindering the Development of Solid State Li Ion Batteries," *iopscience.iop.org*, vol. 164, no. 7, pp. A1731–A1744, 2017, doi: 10.1149/2.1571707jes.
- [32] A. Sharafi, C. Haslam, ... R. K.-J. of M., and undefined 2017, "Controlling and correlating the effect of grain size with the mechanical and electrochemical properties of Li₇La₃Zr₂O₁₂ solid-state electrolyte," *pubs.rsc.org*.
- [33] K. Miyawaki, M. Kishimoto, H. Iwai, ... M. S.-J. of P., and undefined 2014, "Comprehensive understanding of the active thickness in solid oxide fuel cell anodes using experimental, numerical and semi-analytical approach," *Elsevier*,
- [34] W. Xia *et al.*, "Reaction mechanisms of lithium garnet pellets in ambient air: The effect of humidity and CO₂," *Wiley Online Libr.*, vol. 100, no. 7, pp. 2832–2839, Jul. 2017, doi: 10.1111/jace.14865.
- [35] J. Gai *et al.*, "Improving the Li-ion conductivity and air stability of cubic Li₇La₃Zr₂O₁₂ by the co-doping of Nb, Y on the Zr site," *Elsevier*,

- [36] R. P. Campos, A. C. Cuevas, and R. E. Muñoz, “Materials characterization,” *Mater. Charact.*, pp. 1–223, 2015, doi: 10.1007/978-3-319-15204-2.
- [37] H. Geng *et al.*, “Formation mechanism of garnet-like $\text{Li}_7\text{La}_3\text{Zr}_2\text{O}_{12}$ powder prepared by solid state reaction,” *Xiyou Jinshu Cailiao Yu Gongcheng/Rare Met. Mater. Eng.*, vol. 45, no. 3, pp. 612–616, Mar. 2016, doi: 10.1016/s1875-5372(16)30081-9.
- [38] M. Keller, G. Appetecchi, G. Kim, ... V. S.-J. of P., and undefined 2017, “Electrochemical performance of a solvent-free hybrid ceramic-polymer electrolyte based on $\text{Li}_7\text{La}_3\text{Zr}_2\text{O}_{12}$ in P (EO) 15LiTFSI,” *Elsevier*.
- [39] G. Larraz, A. Orera, and M. L. Sanjuán, “Cubic phases of garnet-type $\text{Li}_7\text{La}_3\text{Zr}_2\text{O}_{12}$: the role of hydration,” *J. Mater. Chem. A*, vol. 1, no. 37, p. 11419, Oct. 2013, doi: 10.1039/c3ta11996c.
- [40] D. Kobor, B. Guiffard, L. Lebrun, ... A. H.-J. of P. D., and undefined 2007, “Oxygen vacancies effect on ionic conductivity and relaxation phenomenon in undoped and Mn doped PZN-4.5 PT single crystals,” *iopscience.iop.org*,
- [41] S. R. Elliott, “A.c. conduction in amorphous chalcogenide and pnictide semiconductors,” *Adv. Phys.*, vol. 36, no. 2, pp. 135–217, Jan. 1987, doi: 10.1080/00018738700101971.
- [42] R. H. Chen, R. Y. Chang, C. S. Shern, and T. Fukami, “Structural phase transition, ionic conductivity, and dielectric investigations in $\text{K}_3\text{H}(\text{SO}_4)_2$ single crystals,” *J. Phys. Chem. Solids*, vol. 64, no. 4, pp. 553–563, Apr. 2003, doi: 10.1016/S0022-3697(02)00310-4.
- [43] L. Dhivya, N. Janani, B. Palanivel, and R. Murugan, “ Li^+ transport properties of W substituted $\text{Li}_7\text{La}_3\text{Zr}_2\text{O}_{12}$ cubic lithium garnets,” *AIP Adv.*, vol. 3, no. 8, Aug. 2013, doi: 10.1063/1.4818971.
- [44] N. Murali, S. Margarete, V. Rao, V. V.-J. of Science, and undefined 2017,

“Structural, impedance, dielectric and modulus analysis of $\text{LiNi}_{1-x-y}\text{Mg}_x\text{Zn}_y\text{O}_2$ cathode materials for lithium-ion batteries,” *Elsevier*.

- [45] D. Kobor, O. Bodian, W. Bodian, A. K. Diallo, and M. Tine, “Structural and impedance characterization of ceramics prepared from NPK fertilizer,” *Process. Appl. Ceram.*, vol. 9, no. 2, pp. 107–115, 2015, doi: 10.2298/PAC1502107K.

DECLARATION

We hereby certify that the work which is presented in the Major Project –II entitled in fulfillment of the requirement for the award of the Master of Science in **Physics** and submitted to the Department of **Applied Physics**, Delhi Technological University, Delhi is an authentic record of our own, carried out during a period from August 2020 to May 2021 under the supervision of **Dr. Amrish K. Panwar**.

The matter presented in this report/thesis has not been submitted by us for the award of any other degree of this or any other Institute/University. The work has been accepted in SCI/SCI expanded/SSCI/Scopus indexed journal OR peer-reviewed Scopus indexed conference with the following details:

Title of paper: Investigation of structural, electrical and dielectric properties of $\text{Li}_7\text{La}_3\text{Zr}_2\text{O}_{12}$ (LLZO) synthesized by solid state reaction route.

Author names (in sequence as per research paper): Ujjawal Sigar, Sharad Singh Jadaun and Amrish K. Panwar

Name of Conference/Journal: 6th International Conference on Advanced Production and Industrial Engineering(ICAPIE) - 2021

Conference Dates with venue(if applicable): Jun 18-19, 2021

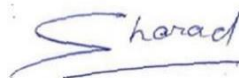
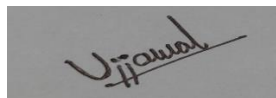
Have you registered for conference(Yes/No)?: Yes

Status of paper(Accepted/Published/Communicated): Accepted

Date of paper communication: 25 Apr 2021

Date of paper acceptance: 13 May 2021

Date of paper publication: October 2021



Name(Roll No): Ujjawal Sigar(2K19/MSCPHY/11), Sharad Singh Jadaun(2K19/MSCPHY/09)

SUPERVISOR CERTIFICATE

To the best of my knowledge, the above work has not been submitted in part or full for any Degree or Diploma to this University or elsewhere. I further certify that the publication and indexing information given by student(s) is correct.

Place: New Delhi

Date: 30 May 2021



(SUPERVISOR SIGNATURE)

Plagiarism Report



Disset_shard.docx

May 31, 2021

5073 words / 28564 characters

Disset_shard.docx

Sources Overview

3%

OVERALL SIMILARITY

1	mafiadoc.com INTERNET	<1%
2	nsp.naturalspublishing.com INTERNET	<1%
3	scholarbank.nus.edu.sg INTERNET	<1%
4	Sayantana Sil, Mrinmay Das, Joydeep Datta, Soumi Halder, Partha Pratim Ray. "Impedance Spectroscopy Study of Hydrothermally Synt... CROSSREF	<1%
5	Higher Education Commission Pakistan on 2020-10-15 SUBMITTED WORKS	<1%
6	digitalcommons.fiu.edu INTERNET	<1%
7	open.library.ubc.ca INTERNET	<1%
8	CSU, San Jose State University on 2020-11-01 SUBMITTED WORKS	<1%
9	National University of Singapore on 2014-04-11 SUBMITTED WORKS	<1%
10	Rajesh Narayana Perumal, Venkatraj Athikesavan. " Influence of lanthanides (Ln = La, Nd, and Y) in [Ba Ln] [Zr Ti]O lead-free piezoele... CROSSREF	<1%
11	raiith.iith.ac.in INTERNET	<1%
12	tus.repo.nii.ac.jp INTERNET	<1%

Excluded search repositories:

- None

Excluded from Similarity Report:

- Bibliography
- Small Matches (less than 10 words).

Excluded sources:

- None

Registration Proof

ICAPIE 2021

Program name

6th International Conference on Advanced Production and Industrial Engineering

Program Description

June 18-19, 2021

Fees breakup(Round 2) :

Students(UG/PG/Ph.D) : 6000

Faculty : 7500

Delegates from Industry/R& D Centers : 8000

Fee beyond 10 pages : 500/page

Name of the organizer:

Centre for Advanced Production and Industrial Engineering Research (CAPIER) ,Delhi Technological University, Delhi

Contact Us:

✉ icapie.dtu@gmail.com



₹ 6500.00

Payment Successful!

Thank you for registration in ICAPIE 2021.

Share Your Experience



Payment ID: pay_H5Wz9ygClSCA9

A confirmation email has been sent to you

Acceptance Record



Certificate

Dear Author(s): Ujjawal Sagar, Sharad Singh Jadaun and Amrish K. Panwar

Paper ID: 376

Paper Title: Investigation of structural, electrical and dielectric properties of $\text{Li}_7\text{La}_3\text{Zr}_2\text{O}_{12}$ (LLZO) synthesized by solid state reaction route

This is to enlighten you that the above manuscript has been appraised by the editors of LNME and is accepted for the **6th International Conference on Advanced Production and Industrial Engineering (ICAPIE)- 2021 to be held during June 18-19, 2021**. The paper is recommended for publication in **Lecture Notes in Mechanical Engineering (Scopus Indexed publication of Springer Nature), ISSN: 2195-4356**. The manuscript has been submitted to Springer in May 2021 and will be online during October 2021.

Finally, the team of CAPIER DTU and ICAPIE-2021 would like to extend congratulations to you.

Prof. Ranganath M Singari
(Conference Chair, ICAPIE-2021)

Dr. Harish Kumar
(Convener, ICAPIE-2021)

Research Paper

Investigation of structural, electrical and dielectric properties of $\text{Li}_7\text{La}_3\text{Zr}_2\text{O}_{12}$ (LLZO) synthesized by solid state reaction route

Ujjawal Sigar¹, Sharad Singh Jadaun¹ and Amrish K. Panwar¹

¹Department of Applied Physics, Delhi Technological University, Delhi -110042
Correspondance :ujjawalsigar@gmail.com, sharadjadaun2019@gmail.com
amrish.phy@dtu.ac.in

Abstract. In this study, $\text{Li}_7\text{La}_3\text{Zr}_2\text{O}_{12}$ (LLZO) has been synthesized using a solid-state reaction route at low sintering temperature. X-ray diffraction (XRD) analysis confirms the formation of a mixed phase of tetragonal garnet and cubic structure with a space group of $I41/acd:2$ and $Ia-3d$ respectively. Therefore, the structural, physico-chemical, electrical, and dielectric characterization of synthesized LLZO are performed. The average crystallite size and strain have been estimated from the XRD peaks using the Williamson-Hall method. Field Emission Scanning Electron Microscope (FE-SEM) micrographs reveal slightly agglomerated and dense layer-like staircase kind of morphology in LLZO. The impedance spectroscopy data has been recorded at various temperatures from 313K to 393K over a frequency range of 70kHz to 5MHz. Electrical analysis indicates that charges possess the Classical Hopping mechanism for conduction. A.C. activation energy of LLZO is observed as 0.16 eV at a lower frequency of 70 kHz. Dielectric results show the presence of space charge polarization in the external electric field which consists of hoping polarization in the bulk and interfacial polarization (Maxwell-Wagner polarization) at the grain boundaries.

Keywords: Solid electrolyte, dielectrics, Impedance spectroscopy, polarization.

1 Introduction

In today's information-rich society, lithium-ion batteries have a great impact on the electric automobile market and they are used as energy-storing devices for various purposes. Lithium-ion batteries are in high demand due to their high volumetric, gravimetric energy density, and long cycle life in contrast to various other battery systems [1]–[4]. However, the performance of lithium-ion batteries has some drawbacks when liquid electrolytes are used because of their high flammability and thermal as well as electrochemical instability [4]–[6]. Since the performance of liquid electrolytes is limited with high-capacity metallic anodes and high voltage cathodes [4][7]. Li anodes in liquid electrolytes lead to battery degradation due to their low coulombic efficiency and dendrite formation [4][8]. Hence, there is the utmost need to replace the

liquid electrolyte with a solid-state electrolyte to overcome the problems that occurred due to liquid electrolyte. Therefore, a conventional solid-state electrolyte must have reasonable ionic conductivity with negligible electronic conductivity and good electrochemical and mechanical stability [4][9][10]. Earlier investigations have shown that $\text{Li}_7\text{La}_3\text{Zr}_2\text{O}_{12}$ (LLZO) is a widely accepted inorganic solid-state electrolyte due to its high Li-ion conductivity, good chemical stability, and wider electrochemical potential stability window (more than 5V vs. Li^+/Li) [4][9][11]–[13].

In general, LLZO shows three phases such as cubic at low temperature, tetragonal and cubic at high temperatures [14]–[19]. Earlier, synthesis of LLZO has been attempted through different routes such as solid-state reaction, sol-gel method, pechini method, combustion method, chemical co-precipitation [20]. Among all these methods, the solid-state method is preferred over other methods because of its mass production capability and simple processing. Although, in this process, lithium is lost due to evaporation at high-temperature sintering which influences the conductivity of lithium-ion in $\text{Li}_7\text{La}_3\text{Zr}_2\text{O}_{12}$ (LLZO). Meanwhile, relative density can be enhanced at high sintering temperatures [21]. Therefore to get better performance in the solid-state method both the parameters should be balanced.

In this study, synthesis of the intermediate phase of LLZO as tetragonal garnet and cubic has been carried out at low temperature. XRD and FE-SEM are studied for phase and microstructural investigation, respectively. A.C. Impedance analysis has been performed to explain the electrical and dielectric properties of synthesized LLZO.

2 Experimental

2.1 Material synthesis

Synthesis of LLZO has been carried out by the solid-state reaction route. The stoichiometric ratio of precursors of Li_2CO_3 (CDH make, purity >99%), La_2O_3 (Sigma Aldrich make, purity >99.9%), ZrO_2 (Sigma Aldrich make, purity >99%) were used for ball milling. Since at high-temperature LLZO losses lithium, to compensate for this, additional 10% Li_2CO_3 , was incorporated. All precursors were mixed via Ball Milling in an ethanol medium using steel balls. After ball milling, the powder was dried at 60 °C to remove moisture and then transferred to a furnace where it is calcined in the air atmosphere at 700 °C for 10 hrs. Further, the powder was pressed in the hydraulic machine to make pellets of diameter 10 mm at a pressure of 60 MPa. These pellets were then dried at 80 °C temperature to remove any remaining moisture.

2.2 Material Characterization

Thermogravimetric (TGA) and Thermal differential analysis (TGA) measurements were obtained by PerkinElmer make model: TGA 4000 system. Identification of structure and phase composition of the synthesized LLZO powder has been carried by

Bruker make D-8, X-Ray diffractometer in conjunction with $\text{CuK}\alpha$ as a source of radiation of wavelength, 1.54\AA . A wide scan range pattern of LLZO powder was recorded for the diffraction angle of $10\text{--}80^\circ\text{C}$ with a step size of 0.02° . The morphology of the sample was examined using FEI make Nova NanoSEM 450 at an operating voltage of 15 kV. AC impedance spectroscopy of LLZO pellets was obtained by HIOKI make 3532 LCR oscilloscope in the high-frequency range of 72 kHz to 5 MHz within the temperature range 30°C and 100°C to record four parameters such as R_p (Parallel resistance), C_p (Parallel capacitance), D (Dissipation factor), and Z (Total Impedance). Both the surfaces of the Pellet were polished with Silver paste to make them conductive. The obtained pellets were dried at 80°C for 30 min. Complex Impedance (Z^*), Real part (Z'), and Imaginary part (Z'') of Impedance are related to each other as $Z^* = Z' + jZ''$. Here Z'' and Z' can be determined using the following equations.

$$Z'' = \frac{2\pi R_p^2 C_p f}{1 + R_p^2 C_p^2 4\pi^2 f^2} \quad (1)$$

$$Z' = \frac{R_p}{1 + R_p^2 C_p^2 4\pi^2 f^2} \quad (2)$$

Other frequency related properties of LLZO can be explained by the Complex Dielectric Constant (ϵ^*), Dielectric Constant (ϵ'), Dielectric Loss (ϵ'') and Dissipation factor ($\tan\delta$). These parameters are related to each other as $\epsilon^* = \epsilon' + j\epsilon''$. The real part of the complex dielectric was calculated from.

$$\epsilon' = \frac{C_p d}{A\epsilon_0} \quad (3)$$

Where C_p = Parallel capacitance, d = thickness of pellet, A = Area of pellet, ϵ_0 = permittivity of free space.

$$\tan\delta = \frac{\epsilon''}{\epsilon'} \quad (4)$$

Further, A.C. conductivity is calculated using the given relation:

$$\sigma_{a.c.} = \omega\epsilon_0\epsilon'' \quad (5)$$

3 Results and Discussions

3.1 Thermal Analysis

DTA/TG analysis is required for selecting the optimum calcination temperature to study the phase transition of the ball-milled raw material. In this work, thermal analysis curves of an as-synthesized LLZO sample are obtained by calcinating it in the air atmosphere. TGA curve shows the four-stage mass loss curve. Analysis of the TGA curve revealed that there is 0.581% weight loss in the material up to 100°C

which depicts that moisture is removed from the raw material and further reacted with La_2O_3 to form $\text{La}(\text{OH})_3$ [22]. Here, two endothermic peaks are detected at 335.87 °C and 446.91 °C in between the temperature range of 300 – 500 °C. The first endothermic peak can be explained by the decomposition of La_2O_3 to form intermediate compound LaOOH and H_2O is released as a byproduct [22]. Further, LaOOH reacts with CO_2 to form La_2O_3 and releases CO_2 at 446.91 °C [22]. The carbonates start decomposing above 600 °C [23][24]. During the transition temperature from 630 °C to 750 °C, there is a 4.2% weight loss in the material which reveals that Li_2CO_3 starts decomposing by releasing CO_2 and hence, it leads to the formation of a mixed-phase of LLZO. Further, the strong endothermic peak of DTA curve at 845 °C shows the formation of the tetragonal phase. Therefore, the sample is calcinated at 700 °C to get intermediate phase i.e. Mixture of Tetragonal garnet and Cubic, as confirmed by XRD results.

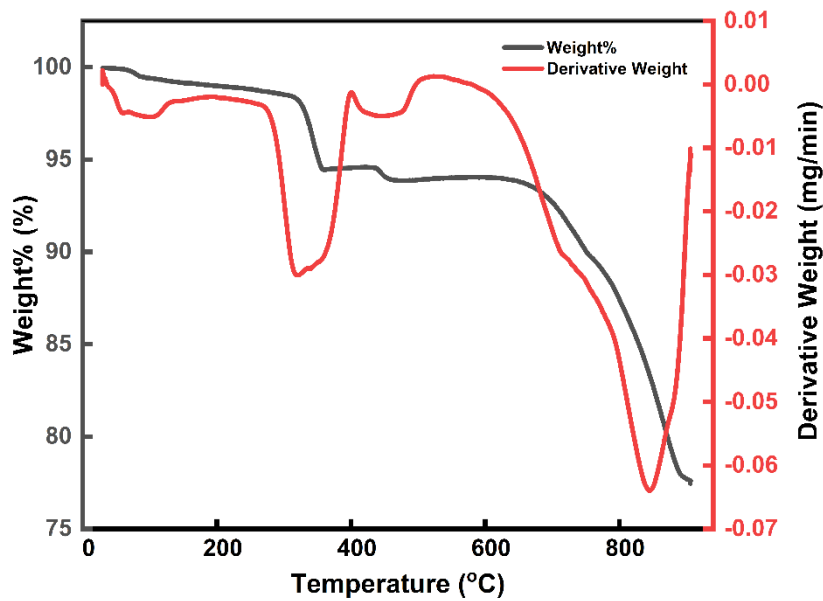


Fig. 1. TGA and DSC curves of LLZO.

3.2 Structural and Morphological Analysis

XRD analysis of an as-synthesized sample of LLZO is shown in fig.2(a). The obtained XRD pattern is almost identical with the Standard XRD pattern of Cubic structure with space group, $Ia-3d$, (DB Card Number 01-080-6067) and Tetragonal garnet structure of space group, $I41/acd:2$, (DB Card Number 01-084-7683) as mixed

phases of LLZO, (PDF- 4+2020). The lattice constants of tetragonal garnet and cubic structures are $a = 13.11\text{\AA}$, $b = 13.11\text{\AA}$, $c = 12.66\text{\AA}$ and $a = 13.02\text{\AA}$, $b = 13.02\text{\AA}$, $c = 13.02\text{\AA}$, respectively. The indexed peaks shown in the XRD pattern represent the existence of LLZO in two phases simultaneously (Cubic and Tetragonal garnet). In Fig.2(b), the Williamson-Hall plot is used to calculate crystallite size and microstrain from broadening of diffraction peaks by using the following expression.

$$\beta\cos\theta = \frac{K\lambda}{D} + 4\epsilon\sin\theta \quad (6)$$

Here, symbols β , ϵ , D , λ , and K are FWHM, micro-strain, crystallite size, wavelength of X-ray, and constant, respectively.

Intercept and slope of the linearly fitted plot between $\beta\cos\theta$ on Y-axis and $4\sin\theta$ on X-axis (fig 2 b) give crystallite size and microstrain, respectively. Crystallite size and microstrain obtained from the plot is 218nm and 2.93×10^{-4} , respectively.

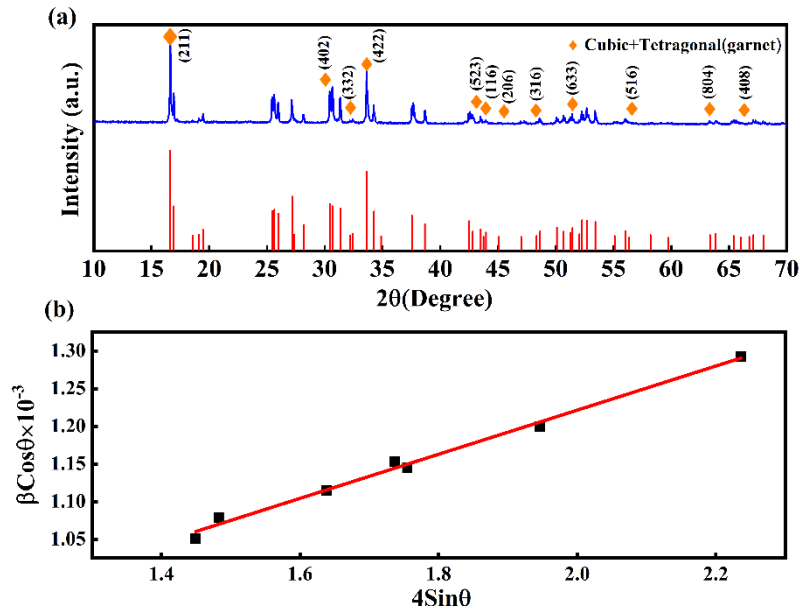


Fig. 2. (a) XRD pattern and (b) Williamson-Hall plot of as-synthesized LLZO at calcination temperature of 700 °C for 6 hrs in air atmosphere.

SEM images of LLZO powder calcinated at 700 °C for 6 hr are shown in Fig.3 at two magnifications of (a) 5 μm and (b) 400nm. The size of particles is directly influenced by the calcination temperature. Fig.3(a) shows that particles are dense and partially agglomerated with irregular morphology in this intermediate stage of LLZO. This agglomeration is due to the alteration of one phase to another i.e. Cubic to Tetragonal (garnet), which results in the declination of bulk ionic conductivity of the material. On

further magnifying the features observed in the micrograph of Fig.3 (a), a dense layered (staircase-like) morphology is observed at the nano level (Fig 3 (b)).

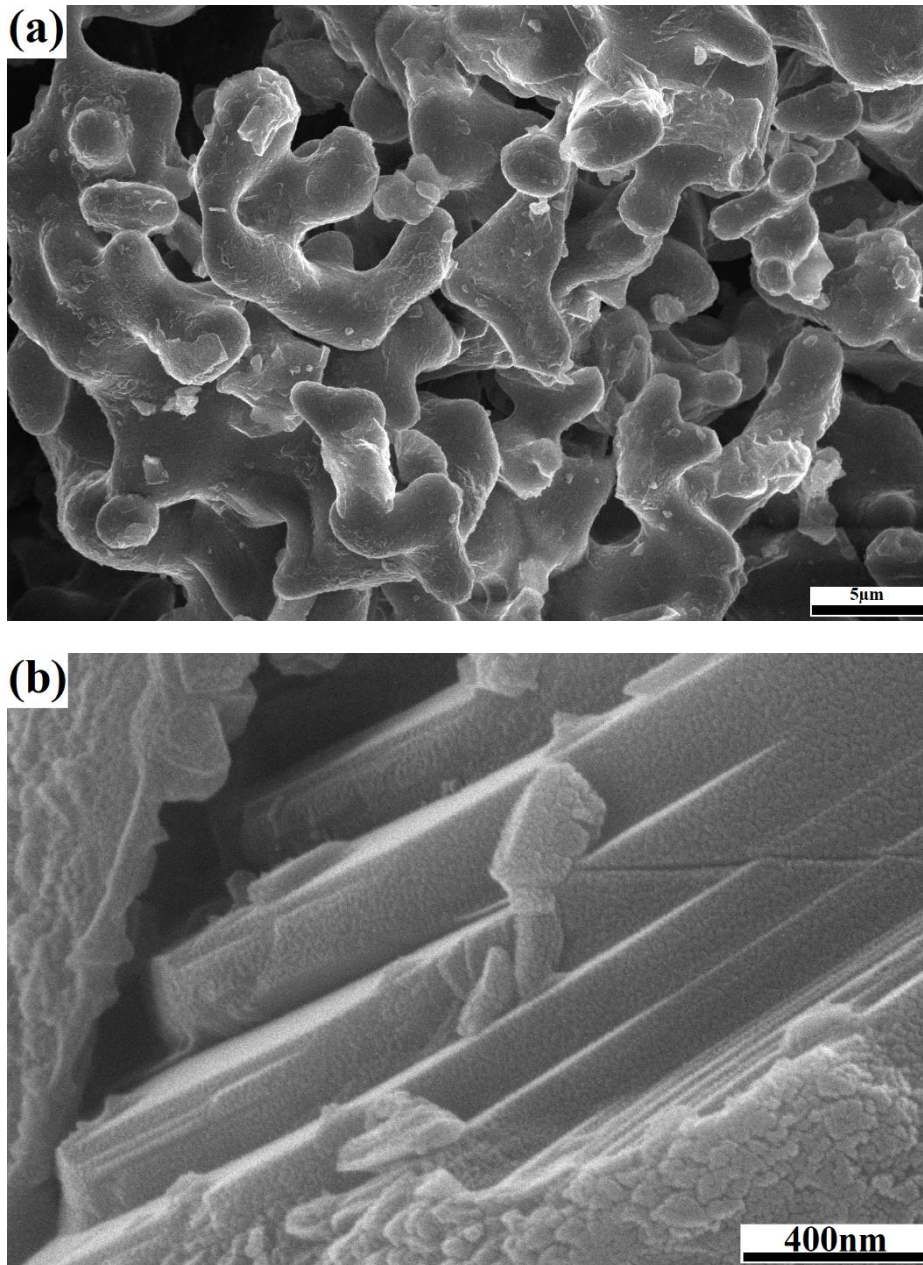


Fig. 3. SEM image of LLZO,(a)5μm (b)400nm.

3.3 Electrical measurement

Dependency of AC conductivity, $\sigma_{a.c}$ on frequency and temperature is shown in Fig.4(a) at logarithmic scale as $\log\sigma_{a.c}$ vs $\log\omega$ for different temperatures from 30 °C to 100 °C for as-synthesized LLZO. The A.C. conductivity increases with an increase in temperature. These curves at various temperatures show two regions. Initially, at low frequency the logarithmic value of a.c. conductivity remains nearly constant. In the high-frequency region, the logarithmic value shows linear dependency on the frequency. Nature of graph can be characterized by using Universal Dynamic Response Equation (the power law, Eq.7 [25]) given as:

$$\sigma_{a.c} = A\omega^n \quad (7)$$

Where the constant A represents the strength of polarization and n is the frequency exponent. The slope and intercept of $\log\sigma_{a.c}$ vs $\log\omega$ plot represent the frequency exponent and the constant A at the corresponding temperature respectively. Therefore n can be written as:

$$n = \frac{\Delta \ln \sigma_{a.c.}}{\Delta \ln \omega} \quad (8)$$

Table 1. Calculated value of n and A at different temperatures.

Temperature(K)	n	A[S/(cm.rad.s)]
303	0.99922	0.000032599
313	0.72772	0.000208945
323	0.587	0.000534826
333	0.57689	0.000658695
343	0.47874	0.00150669
353	0.45657	0.002116482
363	0.44742	0.002550591
373	0.386	0.00478648

Three different phenomena are used to explain the conduction mechanism [26] such as Classical hopping over the barrier, Quantum mechanical tunnelling (QMT), and small polaron tunnelling.

In the QMT model, the expression of n is given by:

$$n = 1 - \frac{4}{\ln \frac{v_{ph}}{\omega}} \quad (9)$$

While for small polaron [27]:

$$n = 1 - \frac{4}{\ln \frac{1}{\omega\tau} \frac{W_H}{kT}} \quad (10)$$

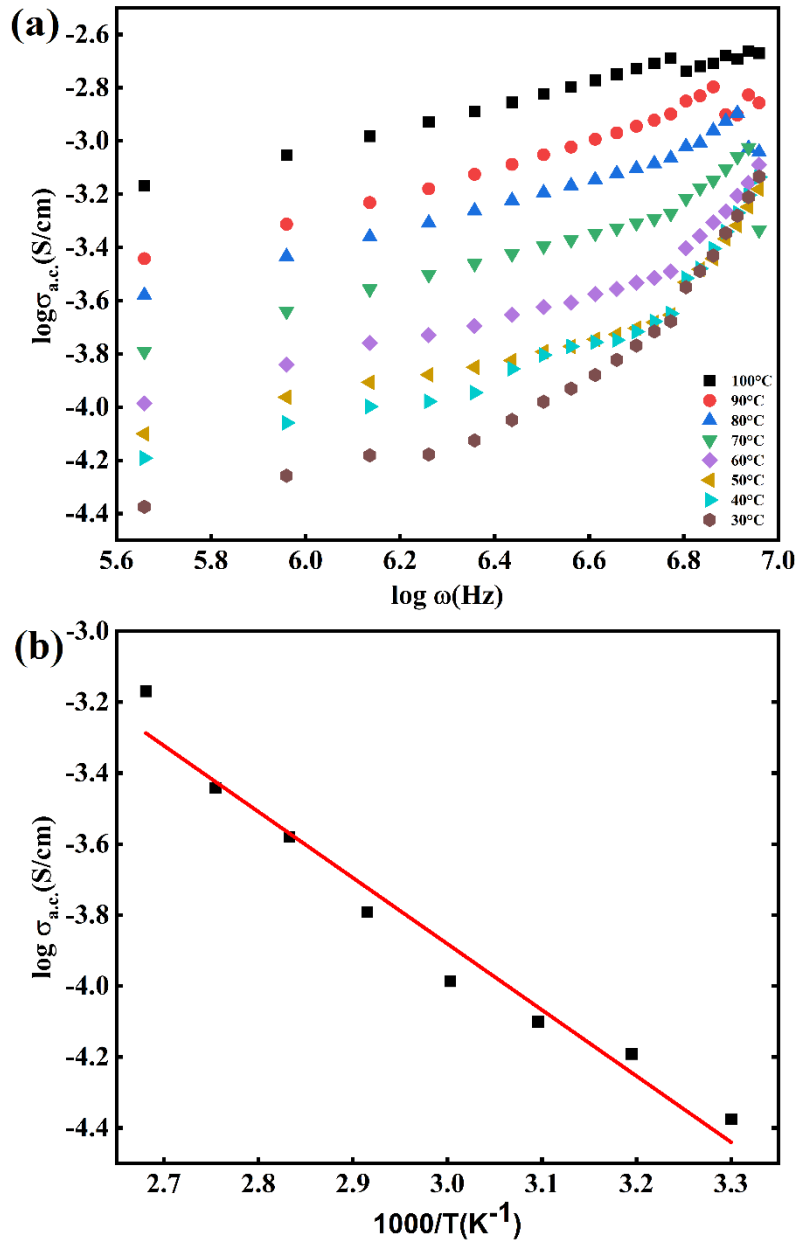


Fig. 4. (a) AC conductivity versus the frequency at the temperature range 30 °C to 100 °C, (b) Arrhenius plot, variation of conductivity with temperature for as-synthesized LLZO.

And for classical hopping:

$$n = 1 - \frac{6kT}{E_0 - kT \ln \frac{v_{ph}}{\omega}} = 1 - \frac{6kT}{E_0 - kT \ln \frac{1}{\omega\tau}} \quad (11)$$

It is clear from Eq. 8 that n is independent of temperature for the QMT model and increases with temperature for small polaron tunneling. Table 1 shows that n is decreasing with an increase in the temperature which points out that the conduction mechanism in the mixed-phase of LLZO is majorly due to Classical hopping.

The activation energy at frequency, 70kHz is calculated from the Arrhenius plot shown in Fig.4(b). The activation energy for the mixed-phase of LLZO is observed as 0.16 eV.

3.4 Dielectric measurement

The calculated value of constant A is shown in table 1. The value of A increases with an increase in the temperature which signifies that polarizability increases with increasing temperature. It has also been confirmed by the dielectric constant as shown in fig.5(a). It clearly shows the dependency of dielectric constant (ϵ') on frequency and temperature. ϵ' is gradually decreasing with increasing frequency which shows dielectric dispersive behavior of mixed-phase of LLZO at low frequencies [28]. This dielectric dispersion phenomenon is also confirming the classical charge hopping mechanism. The higher value of ϵ' at low frequency can be explained by space charge polarisation in which polarization and migration of Li^+ takes place [28] and the existing dipoles in the material orient themselves in the field change. At higher frequencies, ϵ' become nearly constant which can be explained as the inability of the electric dipole to adapt themselves to varying external electric field. On increasing temperature dielectric constant also increases due to the alignment of dipoles along the electric field direction. On applying an electric field across the material, ionic motion starts through classical hopping. Since grain boundaries offer a significant amount of resistance therefore at grain boundaries electrons get stacked up [29] which induces polarization at grain boundaries (Interfacial Maxwell Wagner polarization) [30]. ϵ'' and ϵ' shows a similar type of behavior with frequency. Figure 5(b) indicate that ϵ'' first decreases with frequency and becomes nearly constant at a higher value of frequency. Since a certain amount of electrical energy is absorbed by the dipolar molecules of the material for orienting themselves along the applied field leads to dielectric loss. The increase in ϵ'' with increasing temperature shows the thermal dependence of dielectric relaxation of the material.

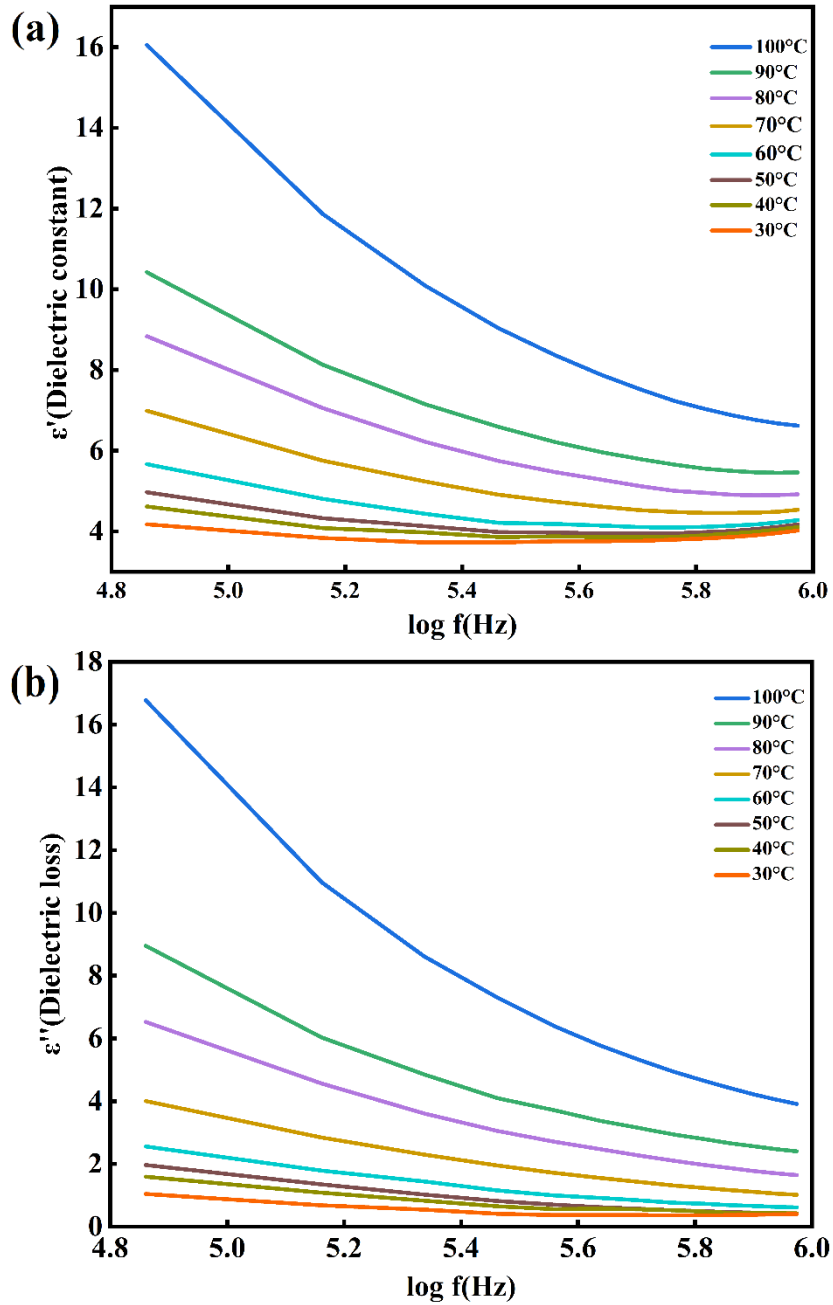


Fig. 5. Dielectric permittivity (a)real and (b)imaginary part versus the logarithm of frequency at various temperatures.

4 Conclusion

$\text{Li}_7\text{La}_3\text{Zr}_2\text{O}_{12}$ (LLZO) has been successfully synthesized using a solid-state reaction route at low sintering temperature. DTA/TGA results indicate that the LLZO phase is formed at 700 °C. XRD results confirm the formation of a mixed phase of tetragonal garnet and cubic as an intermediate form of LLZO. The XRD shows that the material is in crystalline form and has tetragonal(garnet) and cubic-like structure. From the Williamson-Hall method, an average crystallite size of 218nm and a strain of 2.93×10^{-4} are obtained. FESEM images show that the particles are partially agglomerated and have a dense layered (staircase-like) structure. The above data shows the presence of different crystalline phases i.e. tetragonal(garnet) and cubic. The obtained LLZO was used for electrical analysis. The A.C. conductivity of the composite LLZO phase shows a significant dependence on the frequency which can be correlated by UDR. In the temperature region of 313K to 393K, the frequency exponent of the power-law equation confirms that the conduction mechanism is taking place through Classical Hopping and the activation energy at 70kHz is 0.16eV. The dielectric analysis shows that variation of dielectric properties can be explained by space charge polarization i.e. hopping polarization and interfacial polarization (Maxwell Wagner polarization).

The present studies show that mixed-phase LLZO is synthesized at low temperature and its structural, morphological, dielectric, and electric properties were successfully studied.

Acknowledgment. Authors also would like to thanks Delhi Technological University (DTU) to provide a financial project grant “DTU/IRD/619/2019/2114” to explore LIBT Research work. Authors are also thankful to Mr. Abhishek Bhardwaj, Research Scholar, LIBT lab, Applied Physics Department DTU, for his kind help and support to carry out the research work.

References

1. D. Larcher and J. M. Tarascon, “Towards greener and more sustainable batteries for electrical energy storage,” *Nature Chemistry*, vol. 7, no. 1. Nature Publishing Group, pp. 19–29, Jan. 01, 2015, doi: 10.1038/nchem.2085.
2. M. Li, J. Lu, Z. Chen, and K. Amine, “30 Years of Lithium-Ion Batteries,” *Adv. Mater.*, vol. 30, no. 33, p. 1800561, Aug. 2018, doi: 10.1002/adma.201800561.
3. W. Li, B. Song, A. M.-C. S. Reviews, and undefined 2017, “High-voltage positive electrode materials for lithium-ion batteries,” *pubs.rsc.org*.
4. M. Mishra et al., “Ga-doped lithium lanthanum zirconium oxide electrolyte for solid-state Li batteries,” *Electrochim. Acta*, vol. 353, p. 136536, 2020, doi: 10.1016/j.electacta.2020.136536.

5. G. Gachot et al., "Deciphering the multi-step degradation mechanisms of carbonate-based electrolyte in Li batteries," *J. Power Sources*, vol. 178, no. 1, pp. 409–421, Mar. 2008, doi: 10.1016/j.jpowsour.2007.11.110.
6. N. P. Lebedeva and L. Boon-Brett, "Considerations on the Chemical Toxicity of Contemporary Li-Ion Battery Electrolytes and Their Components," *J. Electrochem. Soc.*, vol. 163, no. 6, pp. A821–A830, Feb. 2016, doi: 10.1149/2.0171606jes.
7. B. Wu et al., "The Role of Solid Electrolyte Interphase Layer in Preventing Li Dendrite Growth in Solid-State Batteries The Role of Solid Electrolyte Interphase Layer in Preventing Li Dendrite Growth in Solid-State Batteries †," *pubs.rsc.org*, doi: 10.1039/x0xx00000x.
8. B. Liu, J. Zhang, W. X.-Joule, and undefined 2018, "Advancing lithium metal batteries," Elsevier.
9. A. J. Samson, K. Hofstetter, S. Bag, and V. Thangadurai, "A bird's-eye view of Li-stuffed garnet-type Li₇La₃Zr₂O₁₂ ceramic electrolytes for advanced all-solid-state Li batteries," *Energy Environ. Sci.*, vol. 12, no. 10, pp. 2957–2975, 2019, doi: 10.1039/c9ee01548e.
10. Y. Meesala, A. Jena, H. Chang, and R.-S. Liu, "Recent Advancements in Li-Ion Conductors for All-Solid-State Li-Ion Batteries," *ACS Publ.*, vol. 2, no. 12, pp. 2734–2751, Dec. 2017, doi: 10.1021/acscenergylett.7b00849.
11. S. Afyon, K. Kravchuk, ... S. W.-J. of M., and undefined 2019, "Building better all-solid-state batteries with Li-garnet solid electrolytes and metalloid anodes," *pubs.rsc.org*.
12. Q. Liu et al., "Challenges and perspectives of garnet solid electrolytes for all solid-state lithium batteries," Elsevier.
13. W. Z.-D. Transactions and undefined 2014, "Structural limitations in the family of lithium conducting garnets lead to optimum structural parameters and a maximum attainable conductivity," *pubs.rsc.org*, doi: 10.1039/b000000x.
14. C. Shao, H. Liu, Z. Yu, Z. Zheng, N. Sun, and C. Diao, "Structure and ionic conductivity of cubic Li₇La₃Zr₂O₁₂ solid electrolyte prepared by chemical co-precipitation method," *Solid State Ionics*, vol. 287, pp. 13–16, 2016, doi: 10.1016/j.ssi.2016.01.042.
15. X. Wang et al., "Phase transition and conductivity improvement of tetragonal fast lithium ionic electrolyte Li₇La₃Zr₂O₁₂," Elsevier.
16. J. Awaka, N. Kijima, H. Hayakawa, J. A. solid state chemistry, and undefined 2009, "Synthesis and structure analysis of tetragonal Li₇La₃Zr₂O₁₂ with the garnet-related type structure," Elsevier.
17. "Phase stability of a garnet-type lithium ion conductor Li₇La₃Zr₂O₁₂," *pubs.rsc.org*.
18. S. Toda, K. Ishiguro, Y. Shimonishi, A. Hirano, Y. T.-S. S. Ionics, and undefined 2013, "Low temperature cubic garnet-type CO₂-doped Li₇La₃Zr₂O₁₂," Elsevier.
19. Y. Wang, W. L.-J. of P. Sources, and undefined 2015, "Phase transition in lithium garnet oxide ionic conductors Li₇La₃Zr₂O₁₂: The role of Ta substitution and H₂O/CO₂ exposure," Elsevier.
20. S. Ramakumar, C. Deviannapoorani, L. Dhivya, L. S. Shankar, and R. Murugan, "Lithium garnets: Synthesis, structure, Li⁺ conductivity, Li⁺ dynamics and applications," *Prog. Mater. Sci.*, vol. 88, pp. 325–411, 2017, doi: 10.1016/j.pmatsci.2017.04.007.
21. W. Xue et al., "The effect of sintering process on lithium ionic conductivity of Li_{6.4}Al_{0.2}La₃Zr₂O₁₂ garnet produced by solid-state synthesis," *RSC Adv.*, vol. 8, no. 24, pp. 13083–13088, 2018, doi: 10.1039/c8ra01329b.
22. H. Geng et al., "Formation mechanism of garnet-like Li₇La₃Zr₂O₁₂ powder prepared by solid state reaction," *Xiyou Jinshu Cailiao Yu Gongcheng/Rare Met. Mater. Eng.*, vol. 45, no. 3, pp. 612–616, 2016, doi: 10.1016/s1875-5372(16)30081-9.

23. M. Keller, G. Appetecchi, G. Kim, ... V. S.-J. of P., and undefined 2017, "Electrochemical performance of a solvent-free hybrid ceramic-polymer electrolyte based on $\text{Li}_7\text{La}_3\text{Zr}_2\text{O}_{12}$ in P (EO) 15LiTFSI," Elsevier.
24. G. Larraz, A. Orera, and M. L. Sanjuán, "Cubic phases of garnet-type $\text{Li}_7\text{La}_3\text{Zr}_2\text{O}_{12}$: the role of hydration," *J. Mater. Chem. A*, vol. 1, no. 37, p. 11419, Oct. 2013, doi: 10.1039/c3ta11996c.
25. D. Kobor, B. Guiffard, L. Lebrun, A. Hajjaji, and D. Guyomar, "Oxygen vacancies effect on ionic conductivity and relaxation phenomenon in undoped and Mn doped PZN-4.5PT single crystals," *J. Phys. D. Appl. Phys.*, vol. 40, no. 9, pp. 2920–2926, May 2007, doi: 10.1088/0022-3727/40/9/038.
26. S. R. Elliott, "A.c. conduction in amorphous chalcogenide and pnictide semiconductors," *Adv. Phys.*, vol. 36, no. 2, pp. 135–217, Jan. 1987, doi: 10.1080/00018738700101971.
27. R. H. Chen, R. Y. Chang, C. S. Shern, and T. Fukami, "Structural phase transition, ionic conductivity, and dielectric investigations in $\text{K}_3\text{H}(\text{SO}_4)_2$ single crystals," *J. Phys. Chem. Solids*, vol. 64, no. 4, pp. 553–563, Apr. 2003, doi: 10.1016/S0022-3697(02)00310-4.
28. L. Dhivya, N. Janani, B. Palanivel, and R. Murugan, "Li⁺ transport properties of W substituted $\text{Li}_7\text{La}_3\text{Zr}_2\text{O}_{12}$ cubic lithium garnets," *AIP Adv.*, vol. 3, no. 8, Aug. 2013, doi: 10.1063/1.4818971.
29. N. Murali, S. Margarete, V. Rao, V. V.-J. of Science, and undefined 2017, "Structural, impedance, dielectric and modulus analysis of $\text{LiNi}_{1-x}\text{y}-0.02\text{Mg}_0.02\text{Co}_x\text{Zn}_y\text{O}_2$ cathode materials for lithium-ion batteries," Elsevier.
30. D. Kobor, O. Bodian, W. Bodian, A. K. Diallo, and M. Tine, "Structural and impedance characterization of ceramics prepared from NPK fertilizer," *Process. Appl. Ceram.*, vol. 9, no. 2, pp. 107–115, 2015, doi: 10.2298/PAC1502107K.